Flow Turbulence Combust (2018) 101:895–926
https://doi.org/10.1007/s10494-018-9910-x

Large Eddy Simulation of a Novel Gas-Assisted Coal Combustion Chamber

Robert Knappstein[1] · Guido Kuenne[1] · Lukas G. Becker[2] · Francesca di Mare[3] · Amsini Sadiki[1] · Andreas Dreizler[2] · Johannes Janicka[1]

Received: 20 December 2017 / Accepted: 1 April 2018 / Published online: 2 May 2018

Abstract In this work a recently presented combustion chamber that is specifically designed for the investigation of gas-assisted coal combustion and the validation of models is simulated under reactive conditions for the first time. In the configuration coal combustion is assisted and stabilized by a methane flame. In the course of the investigation, the configuration's complexity is increased successively. Results of the isothermal single-phase flow are discussed first. Subsequently, reproducibility of the single-phase methane flame by means of the applied modeling approach is evaluated. In a further step, coal particles having the same thermal power as the methane flame are injected into the configuration. Particle histories, the conversion of the coal particles as well as its retroactive effect on the gas phase are investigated. Experimental results based on laser diagnostics are provided for all operating points and used for comparison with numerical results. Gas phase velocity fields for all operating points are available. In order to identify the reaction in the reactive single-phase case planar laser induced fluorescence of the OH-radical (OH-PLIF) was applied. Overall good agreement between numerical and experimental results could be obtained. In the Large Eddy Simulation (LES) a Flamelet Generated Manifold (FGM) based model is utilized. The four-dimensional manifold is spanned by two mixture fractions, a reaction progress variable and the enthalpy on which the gas phase chemistry gets mapped onto. Thereby, the model accounts for both, volatiles reaction and char conversion. Furthermore, finite rate chemistry effects as well as non-adiabatic physics are considered.

Keywords Large eddy simulation · Coal combustion · FGM · Tabulated chemistry

✉ Robert Knappstein
knappstein@ekt.tu-darmstadt.de

[1] Institute for Energy and Powerplant Technology, Otto-Berndt-Straße 3, 64287 Darmstadt, Germany

[2] Institute for Reactive Flows and Diagnostics, Otto-Berndt-Straße 3, 64287 Darmstadt, Germany

[3] Chair for Thermal Turbomachines and Aircraft Engines, Universitätsstraße 150, 44801 Bochum, Germany

1 Introduction

The combustion of pulverized coal contributes to a large part to the consumption of primary energy sources worldwide [1]. In order to meet targeted reduction of carbon dioxide emissions, the effective usage of this fuel is mandatory. Therefore, knowledge about its combustion process must be obtained. Particularly, the fuel burnout degree and heat release are important information to judge about a combustion system's technical effectiveness but also about its economic efficiency. As a further example, the formation of nitrogen oxides depends on the flame structure and stoichiometric conditions. In order to reduce their formation and hence, the environmental impact, insight into the mechanisms in combustion chambers must be gained. In this regard, the application of transient combustion simulation techniques such as Large Eddy Simulations (LES) becomes increasingly important. Laboratory-scale coal configurations are often investigated to obtain a deepened understanding of the coal combustion process and to validate coal combustion models. Coal burners of this scale usually feature a gas flame that assists and stabilizes the combustion of the coal particles. For instance, the gas-assisted coal jet flame of the Japanese Central Research Institute of Electric Power Industry (CRIEPI) is a widely examined reference test case in this regard. This burner was fully characterized by means of optical diagnostics in [2]. In particular, particle velocities and temperatures in the flame were recorded simultaneously to the planar laser induced fluorescence signal of the OH-radical (OH-PLIF) and the Mie scattering signal of the coal particles. One of this work's aims was to provide a comprehensive data basis for the validation of numerical simulations. Numerous modeling approaches were evaluated using this configuration (e.g., [3–6]). Furthermore, a comparative study between three different Computational Fluid Dynamics (CFD) codes was carried out at this burner in order to identify differences in the prediction accuracy [7]. Rieth et al. [8] evaluated a multiple mixture fraction flamelet based model. Herein, the model was coupled with a detailed treatment of the particle chemistry for the first time. The same configuration was also investigated in [9] who conducted a state-of-the-art Direct Numerical Simulation (DNS). Generally, the LES technique has established in recent years as it is capable of accounting for transient phenomena. Also, as a result of growing computing capacities LES became more and more affordable even for the simulation of semi-industrial combustion chambers. The applicability of LES to such large configurations was demonstrated by Olenik et al. [10], Rabaçal et al. [11] as well as Rieth et al. [12, 13].

Combustion modeling based on flamelets is already well established in the context of pure gas phase combustion. Recently, flamelet models were also applied to coal being a more complex fuel. In the work of Watanabe et al. [14] an approach was proposed, which employs two different mixture fractions to account for the varying fuel composition evoked by the volatiles release and the char conversion. Later on, this concept was further extended by a third mixture fraction additionally considering moisture that is released from the particle [15]. A flamelet model with two mixture fractions was also proposed by Rieth et al. [8, 12, 13]. Depending on whether the simulated configuration is a gas assisted or a self-preserving coal flame the second mixture fraction accounts either for the gaseous fuel [8] or the char burnout products [12, 13], whereas the first one represents the volatiles. Contributions with regards to particular aspects of flamelet modeling in coal combustion were made by Wen et al. [16–19] as well as Messig et al. [20]. Resolved particle simulations were performed by Vascellari et al. [21, 22] as well as Xu et al. [23], who applied and compared flamelet based models with results obtained by resolved chemistry simulations.

In order to obtain extensive insights into gas-assisted coal combustion, a new laboratory-scale combustion chamber was recently designed. Due to the well defined boundary

conditions and the good optical accessibility that allows for the application of advanced laser diagnostic methods, this configuration is well suited for the investigation of gas-assisted coal combustion and combustion model validation. The burner's geometry featuring a swirl nozzle and a quarl is thereby very similar to a facility designed for oxycoal combustion. Investigations regarding the latter can be found in e.g., [24–29]. An experimental study of single-phase combustion within the new configuration was conducted by Becker et al. [30]. Therein, an analysis of the flow field and the flame is conducted. Up to now only the non-reacting flow was numerically investigated by Doost et al. [31]. The authors analyzed residence times of tracers and statistical moments of the flow for a characterization of the configuration. In the present work this coal combustion chamber is simulated under reactive conditions and numerically investigated for the first time. The computations will be conducted with an LES approach where the chemistry is treated by means of Flamelet Generated Manifold (FGM) tabulation accounting for the volatiles combustion as well as the char burnout. The coal particles are treated by a Lagrangian tracking. This rather macroscopic level of modeling also determines the scope of this work. It enables the simulation of full configurations while it cannot contribute to an in-depth understanding of the small scale processes at the coal particle. Accordingly, contrary to the works that consider the detailed chemical processes of individual particles (e.g., [22, 32]) it is the purpose here to assess the performance of an overall LES approach in predicting a full scale configuration. Therefore, to judge on the individual modeling components, the configuration's complexity is increased successively from single-phase non-reactive over single-phase reactive to two-phase reactive conditions.

The outline is as follows: In Section 2, the numerical methods and the main aspects of the applied modeling approach are outlined. The experimental configuration and its numerical setup are explained in Section 3. Subsequently (Section 4), simulation results are discussed and compared with experimental results, whereby measurement data of the two-phase flow velocity field are used. In Section 5, the main findings are summarized. A final conclusion is given.

2 Theoretical Background and Modeling

Simulations are conducted with the academic CFD-code FASTEST. It is a 3D finite volume code, which uses block-structured, boundary-fitted meshes with hexahedral cells to represent complex geometries. The spatial discretization of the velocity is based on a multidimensional Taylor series expansion with second order accuracy [33]. The TVD-limiter proposed by Zhou et al. [34] ensures boundedness of scalar quantities. Temporal integration of the transport equations is done by using an explicit, three-stage Runge-Kutta scheme of second order. The incompressible, variable density Navier-Stokes equations

$$\frac{\partial \overline{\rho}}{\partial t} + \frac{\partial \left(\overline{\rho}\widetilde{u}_j\right)}{\partial x_j} = \overline{S}_{\mathrm{prt},m}, \tag{1}$$

$$\frac{\partial \left(\overline{\rho}\widetilde{u}_i\right)}{\partial t} + \frac{\partial \left(\overline{\rho}\widetilde{u}_i\widetilde{u}_j\right)}{\partial x_j} = \frac{\partial}{\partial x_j}\left(\tau_{ij} - \tau_{ij}^{\mathrm{sgs}}\right) - \frac{\partial \overline{p}}{\partial x_i} + \overline{\rho} g_i + \overline{S}_{\mathrm{prt},u_i}, \tag{2}$$

are solved, where continuity is satisfied by solving a pressure correction equation within each Runge-Kutta stage. The solver is based on an ILU matrix decomposition and uses the strongly implicit procedure suggested by Stone [35]. Within the LES the subgrid fluxes of

momentum are accounted for by the eddy viscosity approach proposed by Smagorinsky [36] where the model coefficient is obtained by the dynamic procedure of Germano et al. [37] with a modification by Lilly [38]. For the dispersed phase a Lagrangian approach is applied, whereby the interaction with the continuous phase is considered by particle source terms S_{prt}. Particle tracking is done by an adaptive, explicit Runge-Kutta scheme of fourth order [39, 40].

2.1 Combustion modeling

In flamelet based models it is assumed that a turbulent flame can correctly be represented by an ensemble of states found in a set of corresponding laminar flames [41]. This concept was extended by Peters by utilizing mixture fraction and scalar dissipation rate to model non-premixed combustion [42, 43]. The FGM approach that is applied in this work also belongs to this group of models. Its central idea is that premixed laminar one-dimensional flames are computed prior to the actual CFD simulation by using detailed reaction kinetics. These flamelets are then tabulated in dependency of only a few control variables, which fully describe the thermo-chemical state. In turn, only these control variables have to be transported by the LES solver. Initial formulations for premixed laminar flames within the flamelet context go back to de Goey and Thije Boonkkamp [44]. The development of the FGM approach originates from the work of van Oijen [45], van Oijen and de Goey [46] and van Oijen et al. [47]. As it is discussed in Sections 4.2 and 4.3, gas-phase combustion essentially has a premixed character in the investigated configuration. The combustion of volatile matter rather corresponds to a non-premixed regime. However, finite rate chemistry effects are also relevant so that a progress variable approach is appropriate. In this work, a premixed flamelet database is used as it is also capable of adequately describing such regimes [48].

The choice of control variables depends on the physics to be covered. In the present work two mixture fractions f_i, the enthalpy h and a reaction progress variable being Y_{CO2} are taken to span a four-dimensional manifold. With the inclusion of the enthalpy and a reaction progress variable non-adiabatic physics and finite rate chemistry effects are accounted for, respectively. In the investigated configuration coal combustion is assisted by a methane flame. Hence, from a physical point of view there are three kinds of gaseous fuels. These are methane, the volatile matter originating from the coal particles and the gaseous char products. In the model applied in this work, methane and volatile matter are treated as one species. Accordingly, pure methane was taken as volatiles composition which is a surrogate fuel, whose reaction is describable in the context of the applied GRI 3.0 reaction mechanism [49]. Considering the complexity of realistic volatiles being composed of several species, this is a simplifying assumption which was evaluated by using detailed chemical kinetics simulations [32]. Thereby, local differences in the chemistry of the volatiles reaction could be found between a realistic composition and the volatiles assumed to consist of pure methane. However, the global volatiles combustion was almost unaffected with regards to flame structure and burning duration. Hence, the methane stream and the volatiles matter can both be represented by the first mixture fraction. The temperature range of 300-850 K was covered by the chemistry table for unburnt mixing states along the f_1-dimension which was sufficient for large parts of the devolatilization phase. The second mixture fraction treats the gaseous char products being carbon monoxide formed in the particle surface reaction. It is defined as follows

$$f_2 = Z_{\text{C,CO}} + Z_{\text{O,CO}} + Z_{\text{N2,SFR}}. \tag{3}$$

$Z_{C,CO}$ denotes the element mass fraction of C from CO, $Z_{O,CO}$ the element mass fraction of O from CO and $Z_{N2,SFR}$ the element mass fraction of the nitrogen going along with the oxygen consumed in the char reaction. In the model the nitrogen is treated as an inert species taking part in the surface reaction (SFR). Hence, the definition of f_2 represents the following chemical reaction

$$2C(s) + O_2 + \alpha N_2 \longrightarrow 2CO + \alpha N_2, \tag{4}$$

whereby $\alpha = 3.7619$ being the ratio of molar fractions of N2 and O2 in air. This definition in combination with a correspondingly formulated source term in the f_2 transport equation accounts both, for a constant oxidizer composition and for the consumption of oxygen during char conversion. Along this dimension unburnt states having a temperature range of 300-2000 K representing fresh gaseous char products are tabulated. Char conversion essentially takes place consecutive to devolatilization and hence, requires high particle temperatures that are covered by these states. The applied modeling is a novel approach for describing char conversion with tabulated chemistry based on control variable, enthalpy and mixture fractions. A model with a similar formulation of the char mixture fraction was recently proposed by Wen et al. [19]. However, differences to the present work exist. In [19] non-premixed flamelets were employed whereas the present model relies on premixed flamelets. Different enthalpy levels are also considered in [19] by accounting for differently heated fuel states. However, in the present work the full manifold range is covered in terms of enthalpy losses which can become relevant if a bunch of particles quenches the reaction below its extinction limit.

In this work the artificially thickened flame (ATF) model was used. It was initially developed by Butler and O'Rourke [50] as well as O'Rourke and Bracco[51]. Its basic idea is to thicken the flame by a factor $\mathcal{F}$ and make it thereby resolvable on the computational mesh. An efficiency function $\mathcal{E}$ accounts for unresolved wrinkling of the thickened flame. Here, a power-law approach proposed by Charlette et al. [52] is used. In order to avoid the thickening of mixing induced gradients and to apply the thickening procedure only in the reaction zone a dynamic approach was suggested by Légier et al. [53]. Therefore, a flame sensor Ω based upon the normalized reaction progress variable [54] is adopted that dynamically and locally adapts the thickening factor $\mathcal{F}$. The four control variables of the applied FGM approach get thickened. Their transport equations then read

$$\frac{\partial\left(\overline{\rho}\widetilde{f_1}\right)}{\partial t} + \frac{\partial\left(\overline{\rho}\widetilde{u}_j\widetilde{f_1}\right)}{\partial x_j} = \frac{\partial}{\partial x_j}\left(\left[\mathcal{F}\mathcal{E}\frac{\overline{\mu}}{Sc} + (1-\Omega)\frac{\mu_t}{Sc_t}\right]\frac{\partial\widetilde{f_1}}{\partial x_j}\right) + \overline{S}_{\mathrm{prt},f_1}, \tag{5}$$

$$\frac{\partial\left(\overline{\rho}\widetilde{f_2}\right)}{\partial t} + \frac{\partial\left(\overline{\rho}\widetilde{u}_j\widetilde{f_2}\right)}{\partial x_j} = \frac{\partial}{\partial x_j}\left(\left[\mathcal{F}\mathcal{E}\frac{\overline{\mu}}{Sc} + (1-\Omega)\frac{\mu_t}{Sc_t}\right]\frac{\partial\widetilde{f_2}}{\partial x_j}\right) + \overline{S}_{\mathrm{prt},f_2}, \tag{6}$$

$$\frac{\partial\left(\overline{\rho}\widetilde{Y}_{CO2}\right)}{\partial t} + \frac{\partial\left(\overline{\rho}\widetilde{u}_j\widetilde{Y}_{CO2}\right)}{\partial x_j} = \frac{\partial}{\partial x_j}\left(\left[\mathcal{F}\mathcal{E}\frac{\overline{\mu}}{Sc} + (1-\Omega)\frac{\mu_t}{Sc_t}\right]\frac{\partial\widetilde{Y}_{CO2}}{\partial x_j}\right) + \frac{\mathcal{E}}{\mathcal{F}}\overline{\dot{\omega}}_{CO2}, \tag{7}$$

$$\frac{\partial\left(\overline{\rho}\widetilde{h}\right)}{\partial t} + \frac{\partial\left(\overline{\rho}\widetilde{u}_j\widetilde{h}\right)}{\partial x_j} = \frac{\partial}{\partial x_j}\left(\left[\mathcal{F}\mathcal{E}\frac{\overline{\mu}}{Pr} + (1-\Omega)\frac{\mu_t}{Pr_t}\right]\frac{\partial\widetilde{h}}{\partial x_j}\right) + \overline{S}_{\mathrm{prt},h}. \tag{8}$$

Details regarding the model and its implementations in the context of FGM in FASTEST are given in [55, 56]. For an in depth description of the tabulation technique particularly with regards to the inclusion of enthalpy, the reader is referred to [57]. For the flamelet computation the one-dimensional detailed chemistry flame code CHEM1D [58, 59] was used. A Lewis number of one was assumed. The PSIC (Particle Source In Cell) method [60] applies for the particle source terms S_{prt} in Eqs. 1-8.

2.2 Interaction of gaseous and dispersed phase

The temperature of each particle evolves from

$$\frac{\mathrm{d}T_{\mathrm{prt}}}{\mathrm{d}t} = \frac{3\alpha}{c_{\mathrm{p,prt}}\rho_{\mathrm{prt}}\frac{D_{\mathrm{prt}}}{2}} \cdot \left(T - T_{\mathrm{prt}}\right) + \frac{\Delta h_{\mathrm{char}}}{m_{\mathrm{prt}} c_{\mathrm{p,prt}}}. \tag{9}$$

Herein, the heat transfer coefficient α follows from a Nusselt number which is based on the correlation of Ranz and Marshall [61, 62]. T denotes the gas phase temperature at the particle position. The particle heat capacity $c_{p,\mathrm{prt}}$ and the particle density ρ_{prt} were set to 1260 J/ (kg K) and 1200 kg/m^3, respectively. The second term on the right hand side of Eq. 9 represents the particle heat up due to the reaction heat released from the heterogeneous char reaction. It amounts to

$$\Delta h_{\mathrm{char}} = -\dot{m}_{\mathrm{char}} \Delta H_{\mathrm{reac}}. \tag{10}$$

whereby $\Delta H_{\mathrm{reac}} = -9200\,\mathrm{kJ/kg}$. The converted char mass rate $\dot{m}_{\mathrm{char}}$ is detailed below. Thermal radiation is not considered.

For devolatilization a single first order reaction (SFOR) approach is used, which was proposed by Badzioch and Hawksley [63]. It reads

$$\frac{\mathrm{d}Y}{\mathrm{d}t} = \left(Y_0 - Y\right) A T_{\mathrm{prt}}^{b} \exp\left(\frac{-E}{R T_{\mathrm{prt}}}\right). \tag{11}$$

Herein, Y and Y_0 are the current and final volatile yield, respectively. The Arrhenius parameters as well as Y_0 are summarized in Table 1 and were obtained from computations adopting the CPD (Chemical Percolation and Devolatilization) - model [64–66] to the applied Rhenish lignite which is specified in Section 3.

Char conversion is calculated according to the model going back to Baum and Street [67, 68]. Therein, the overall char conversion rate reads

$$\frac{\mathrm{d}m_{\mathrm{char}}}{\mathrm{d}t} = -\pi D_{\mathrm{prt}}^2 \rho \mathcal{R} T \frac{X_{\mathrm{O2}}}{\mathcal{M}_{\mathrm{O2}}} \left(R_{\mathrm{diff}}^{-1} + R_{\mathrm{reac}}^{-1}\right)^{-1}. \tag{12}$$

The diffusion rate coefficient is according to

$$R_{\mathrm{diff}} = \frac{C_{\mathrm{diff}}}{D_{\mathrm{prt}}} \left(\frac{T_{\mathrm{prt}} + T}{2}\right)^{0.75}. \tag{13}$$

The reaction rate coefficient arises to

$$R_{\mathrm{reac}} = A\varphi \exp\left(\frac{-E_{\mathrm{a}}}{\mathcal{R} T_{\mathrm{prt}}}\right). \tag{14}$$

Herein, the coal specific parameters C_{diff}, A, E_{a} were determined experimentally. Details about the measuring technique can be found in [69]. The factor φ accounts for the enlarged reactive surface because of porosity as φ expresses the ratio of the reacting surface (including inner surfaces) to the outer sphere surface. In the context of the experimental coal characterization it was determined to

$$\varphi = \exp\left(-2.622 - 1.78\left(1 - \frac{m_{\mathrm{char}}}{m_{\mathrm{char,0}}}\right)\right). \tag{15}$$

Table 1 Devolatilization kinetic parameters of Rhenish lignite for Eq. 11

Y_0 (−)	A (1/s)	b (−)	E (J/mol)
0.5258	$1.868755 \cdot 10^5$	0	$4.8988 \cdot 10^4$

Table 2 Baum and Street model parameters of Rhenish lignite

Parameter	Value	Unit
A	$1.13 \cdot 10^{0}$	1/s
E_a	$1.49 \cdot 10^{5}$	J/mol
C_{diff}	$8.93 \cdot 10^{-16}$	$m/sK^{0.75}$

Herein, m_{char} and $m_{char,0}$ are the current and the initial char mass, respectively. The model parameters are summarized in Table 2.

3 Experimental Configuration

The investigated coal combustion chamber is a generic test rig featuring a 20 kW assisting methane flame and an additional thermal power of 20 kW from the injected coal particles. One of the configuration's central aspects is the near-nozzle region of the burner whose geometry essentially affects the stabilization of the flame and the combustion of volatiles. Thereby, the geometry of the burner nozzle, the quarl and the expansion to the combustion chamber is tightly oriented at the geometry of the self-sustained coal flame reported in [28].

On the right of Fig. 1, the geometry of the nozzle and the quarl is shown. The nozzle consists of two annular orifices concentrically surrounding a bluff body. Through the inner orifice the primary stream consisting of a rich methane-air mixture is provided. In case of a two-phase flow, the coal particles are injected herein. A swirled oxidizer flow leaves the outer orifice and thereby constitutes the secondary stream. The cone shaped quarl featuring a cone angle of 21° against the vertical axis spatially confines the swirling flame. Its walls are made of quartz glass to allow for optical accessibility. The swirl of the secondary stream is generated in a mixing volume upstream of the nozzle. Four vertical straight channels and four inclined channels that are angled by 45° lead into that mixing volume termed plenum. All channels have rectangular cross sections (straight channels: $7.5 \times 11.5\,mm^2$, inclined

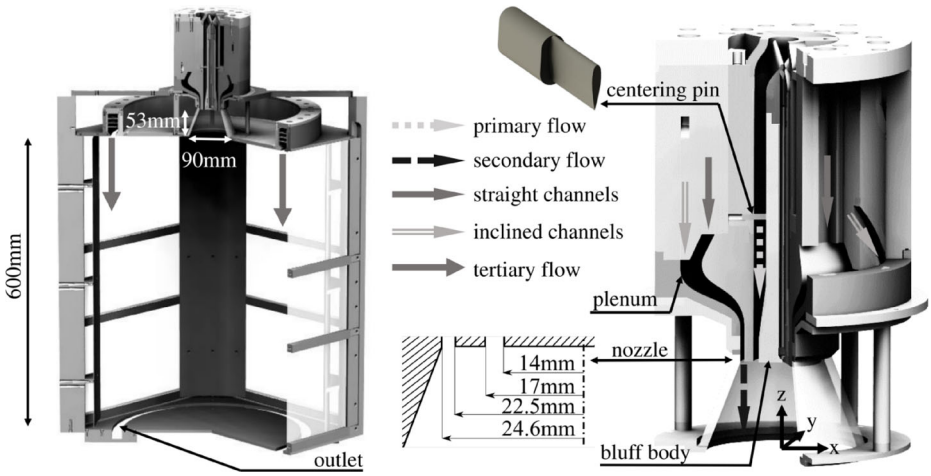

Fig. 1 Left: Optically accessible combustion chamber. Right: Burner assembly consisting of swirl generator, nozzle and quarl

channels: $5 \times 8.5\,\mathrm{mm}^2$). The lower end of the quarl merges with the top of the combustion chamber. There, the coordinate system's origin is located on the configuration's center axis as it is depicted on the right in Fig. 1.

The design of the combustion chamber in the left of Fig. 1 is derived from [28]. Likewise, it is a down-fired flame. The chamber's cross section amounts to $420 \times 420\,\mathrm{mm}^2$. Differently to [28] its length is reduced to 600 mm. Major parts of the surrounding walls are made of quartz glass for an optimized optical accessibility. These windows are plane so that the chamber's cross section is rectangular which is different to the archetypal configuration [28]. However, the corners are rounded. A tertiary stream provides burnout air through an annular orifice directly into the chamber. At the bottom of the chamber, the outlet is also realized as an annular orifice. It prevents backflow and secondary air entrainment into the chamber.

Operating conditions Three operating points are investigated in this work. They are summarized in Fig. 2 and Table 3. Initially, the single-phase non-reactive (SPNR) flow is evaluated. This operating point is investigated with the aim to assess the capability of reproducing the velocity field particularly inside and below the quarl. A snapshot of the instantaneous axial velocity component in the mid section plane of the configuration is given in the left of Fig. 2. It depicts the field of the primary and the secondary stream as well as inside and below the quarl. Schematically, the main axial flow motions are illustrated. Because of the inclination of four out of eight channels leading into the mixing volume the secondary stream has a swirling motion. Due to the inertia of the swirling motion the secondary flow is tightly bounded to the quarl's wall after leaving the annular orifice. Since mass is drawn to the outer regions, a low pressure region forms in the core of the swirling motion which leads to the recirculation of a portion of the flow. As a result of the

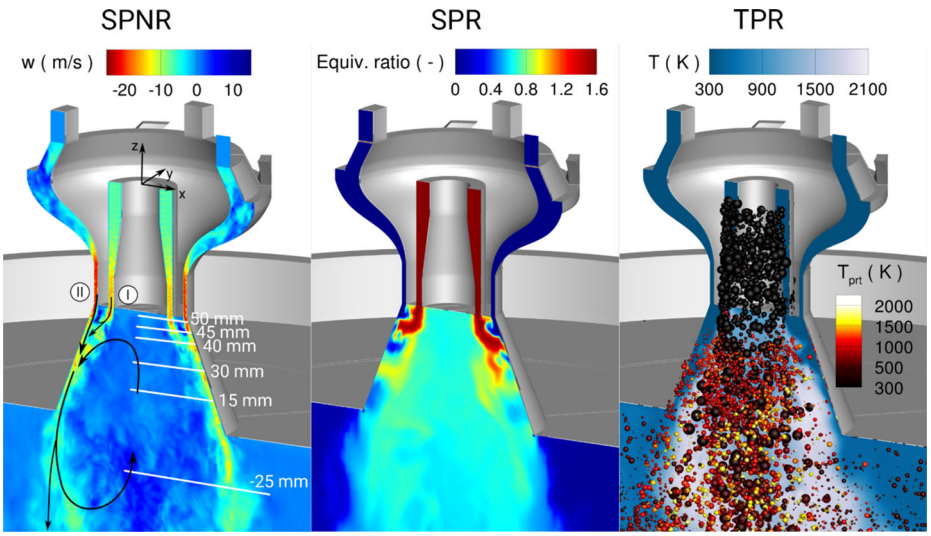

Fig. 2 Mid section planes depicting the three operating points. Left: Instantaneous axial velocity component of single-phase non-reactive flow. I and II indicate the primary and secondary stream, respectively. The black arrows schematically illustrate the main axial flow motions inside and below the quarl. The measuring heights that are taken for comparison are indicated by white lines. The lowest two heights taken in Fig. 5 are not depicted. Middle: Equivalence ratio for single-phase reactive flow. Right: Instantaneous gas phase temperature field on the section plane, individual particles colored by their temperature and sized proportional to their radius. Only every third particle is shown

Table 3 Parameters of the three operating points. I: Primary flow. II: Secondary flow. III: Tertiary flow

	SPNR	SPR	TPR
I Mass flow gas (g/s)	4.775	4.570	4.570
I Mass flow coal particles (kg/h)	–	–	3.25
II Mass flow gas straight channels (g/s)	2.105	2.105	2.105
II Mass flow gas inclined channels (g/s)	4.236	4.236	4.236
III Mass flow gas (g/s)	24.650	24.650	24.650
Equivalence ratio Φ_{I} (only gas phase)	0.0	1.60	1.60
Equivalence ratio $\Phi_{\mathrm{I+II}}$ (only gas phase)	0.0	0.64	0.64

recirculating mass displacement, the primary flow is also quickly drawn to the outer boundaries after entering the quarl. Thereby, another small recirculation zone forms between the annular orifices of primary and secondary stream. Reynolds numbers of primary, secondary and tertiary stream are $Re_{\mathrm{I}} = 5258$, $Re_{\mathrm{II}} = 4597$ and $Re_{\mathrm{III}} = 2163$, respectively. In the second operating point being the single-phase reacting (SPR) flow a thermal power of 20 kW is provided. As it can also be seen in the middle of Fig. 2 and from Table 3 a rich mixture is provided through the primary stream. The swirled secondary flow features an equivalence ratio $\Phi_{\mathrm{II}} = 0$. Inside the quarl, primary and secondary flow form a globally lean mixture. The reaction is analyzed in detail in Section 4.2. For the third operating point being the two-phase reacting (TPR) flow, coal particles are additionally injected into the primary stream. The coal particles potentially provide further 20 kW of thermal power if they are fully burnt. As it is depicted in the right of Fig. 2, smaller particles tend to follow the turbulent swirling motion whereas larger ones leave the nozzle in a more straight direction when they enter the quarl. Due to their different thermal inertia particles are exposed to differing heat up in the hot product gasses of the methane flame reaction which can also be deduced from the right of Fig. 2.

The operating points SPNR and SPR correspond to the cases termed NRAir and RAir in [30], respectively. The particle size distribution applied in the TPR case was determined from laser diffraction analyzes with a lower particle size detection limit of 4.5 μm. From mass balance considerations it could be analyzed that roughly 13 % of the particles are smaller than this limit. The distribution is depicted in Fig. 3. Particles were initialized during the LES by employing a random process which reproduced the particle size distribution. Coal properties are given in Table 4.

Measurement technique In single-phase flow experiments (both, non-reactive and reactive) the flow field was determined using stereoscopic particle image velocimetry (SPIV). In order to identify the reaction in the reactive single-phase case, OH-PLIF was applied. Details regarding these laser diagnostics and their setup can be found in [30]. In the reacting two-phase configuration the velocities of both, gas phase and particles were determined by using a new two-phase PIV measurement technique. Thereby, all sizes of coal particles as shown in Fig. 3 were recorded simultaneously. Within the post-processing the signals of large and small particles are evaluated separately based on an intensity threshold. The resulting velocity vectors of these were attributed to large coal particles and gas phase independent of each other. Strongly correlated statistics could be obtained. However, only the gas phase velocity data were taken for comparison with numerical results in the context of the two-phase flow analysis in this work. A more extensive use of this method's data would

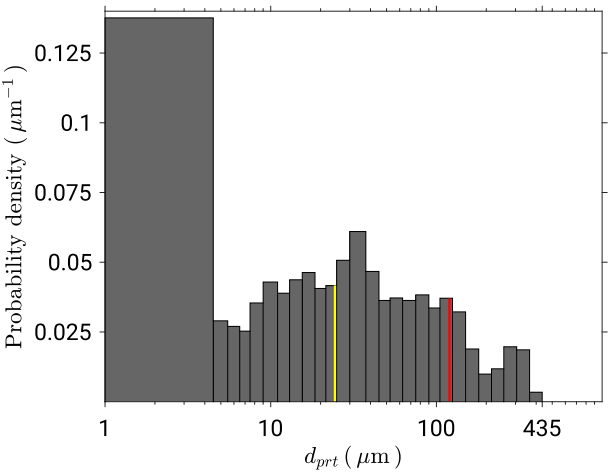

Fig. 3 Experimentally determined coal particle size distribution. The mass averaged mean diameter (red line) and median (yellow line) are at 121.2 μm and 24.3 μm, respectively

require its in-depth description including an error assessment which is beyond the scope of this work.

4 Results

Results of the three operating points are discussed in Sections 4.1-4.3. In Section 4.1, the velocity field is characterized and the appropriateness of boundary conditions in terms of swirl strength is evaluated in order to identify potential sources of error. Section 4.2 is dedicated to the methane flame. Here, a comparison with experimental data allows to judge about the performance of the numerical simulation. Since it significantly contributes to the heat release, its understanding is crucial also for the two-phase reaction. In the latter case, which is discussed in Section 4.3 particles encounter different states which depend on the methane flame and determine the particle reaction.

Table 4 Coal properties of Rhenish lignite. 1: as received, 2: dry and ash free basis

Proximate Analysis[1]	wt. %
Moisture	8.4
Ash	4.1
Volatile Matter	46.6
Fixed Carbon	40.9
Ultimate Analysis[2]	wt. %
Carbon	77.03
Hydrogen	4.85
Oxygen	16.80
Nitrogen	0.98
Sulfur	0.34

4.1 Single-phase non-reactive

For the single-phase non-reactive flow the mass flows of operating point SPNR as specified in Table 3 are applied. All flows – primary, secondary and tertiary – consist of pure air having a temperature of 300 K. The computational mesh consists of approximately 2.5 million cells featuring a cell width $\Delta_{x_i} \approx 0.5$ mm within the quarl and $\Delta_{x_i} \approx 1.0$ - 3.5 mm within the chamber. A time step size of $2.5 \cdot 10^{-6}$ s was applied in order to realize a CFL number (Courant Friedrichs Lewy criterion) below unity for a stable computation. A physical time of 2 s was simulated yielding sufficiently converged statistics in the investigated region. As visible in Fig. 2, significant portions of the nozzle geometry have been included in the computational domain to allow the turbulent flow to naturally develop.

The single-phase non-reactive operating point is investigated mainly for an evaluation of the appropriateness of boundary conditions and for a characterization of the velocity field. Thereby, it is of particular importance to assure that the tangential component of the secondary stream velocity right after leaving the orifice is in agreement with the corresponding experimentally obtained value. This gives information about the swirling strength. If the numerically gained tangential component is lower than the experimental one, it is an indication for numerical diffusion inside the tight nozzle channels.

Results for the three velocity components are depicted in Figs. 4 and 5, respectively, from which a general good agreement between experimental and numerical results with respect to the main flow characteristics can be observed. The two jets leaving the nozzle get

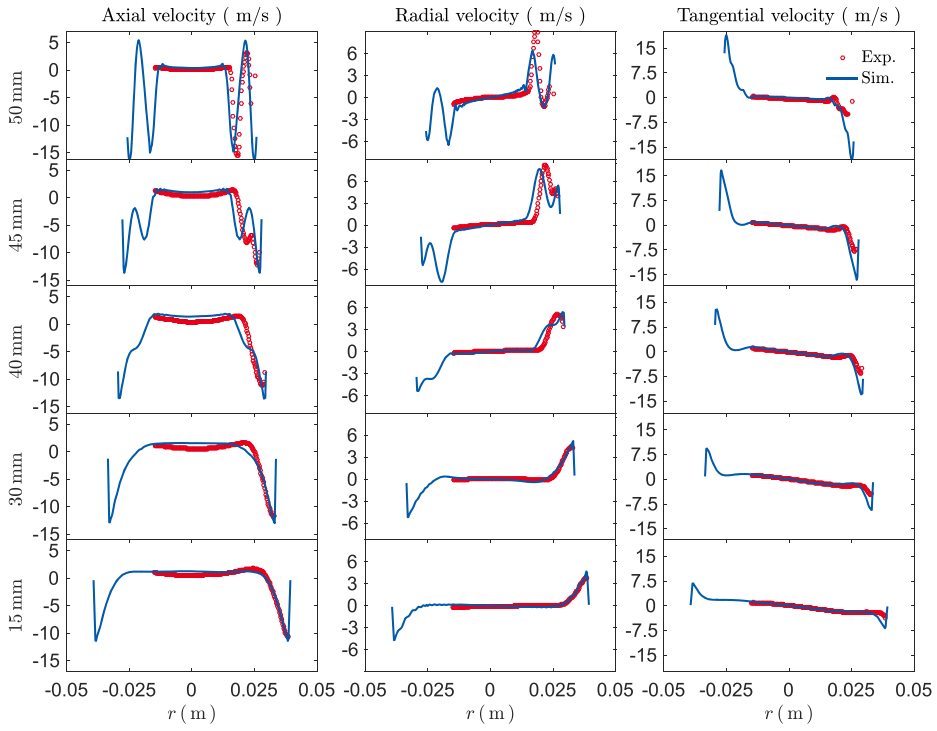

Fig. 4 Comparison of non-reactive single-phase experimental and numerical mean velocity data inside the quarl. The height with respect to the coordinate system's origin is given at the left boarder of each line

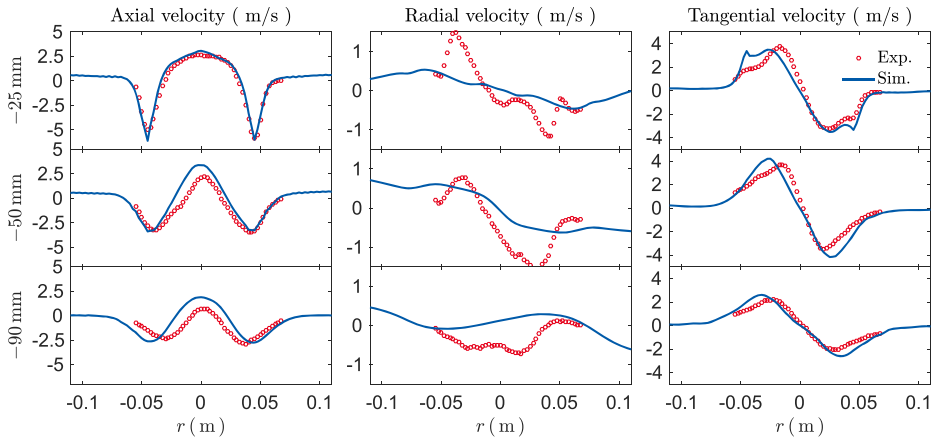

Fig. 5 Comparison of experimental and numerical mean velocity data below the quarl. The height with respect to the coordinate system's origin is given at the left boarder of each line

displaced by the internal recirculation zone and form a swirling motion layer close to the wall. However, taking a closer look to the region close to the annular orifices of primary and secondary stream (e.g., at $z = 45$ mm and $z = 50$ mm) it appears that the experimental data are slightly shifted toward the wall. This mismatch is probably due to an inaccurate mapping of the experimental flow field in that region and was reported in [30]. Keeping that in mind, experimental and simulation results agree to a good degree. At the height of $z = 45$ mm it can be observed that primary and secondary flow have not fully merged in the simulation, yet. However, this process is already ongoing in the experiment at that height. In this flow the tangential velocity representing the strength of the swirling motion is of the same order of magnitude as the axial component. Here, the velocity layer is bounded very close to the wall which induces difficulties in the experiment to correctly measure the out-of-plane component by using stereoscopic PIV. Hence, it cannot be judged precisely on the swirling strength from the experimental data inside the quarl. However, the tangential component below the quarl is well reproduced by the simulation. Concluding from these results there is no indication that the swirl is underestimated due to numerical dissipation in the channels of the burner head. Accordingly, boundary conditions are appropriately set.

Analyzing the flow field below the quarl the axial and the tangential component exhibit a good agreement, so that it can be concluded that the extent of the large recirculation zone is comparable. The radial component is more distinct in the experiment. However, it is rather small and therefore of minor importance. With increasing distance to the quarl experimental and numerical profiles deviate from each other. This might also be due to the fact that the experimentally determined field is not symmetric as it is also reported in [30]. The authors state that this might be the consequence of a not perfectly aligned bluff body in the center of the burner head. Therefore, deviations between experimental and numerical results should not be overrated.

4.2 Single-phase reactive

In this section the swirled methane flame which stabilizes inside the quarl is investigated. It corresponds to the operating point specified as SPR in Table 3. A rich air-methane mixture

is provided by the primary stream. Swirled air is added by the secondary stream and makes the flame globally lean. Wall temperatures were obtained from radiation thermometer measurements and are locally dependent in the range of 320 - 500 K. A physical time of 2.39 s was simulated for sufficiently converged statistics. A time step size of $5 \cdot 10^{-6}$ s was applied which was limited by simulation stability requirements.

A photography of the flame is shown in Fig. 6. Its exposure time was set to 20 s in order to average the wrinkling of the turbulent flame. By referring to the chemiluminescence signal the position and the extent of the reaction zone can be roughly estimated. It can be observed that a main flame forms that encompasses the central recirculation zone inside and below the quarl. At this operating point also a side flame appears that stabilizes between the cold gasses of primary and secondary stream. Hence, it burns detached from the main flame. There is no stabilization support in terms of hot oxygen containing product gasses from the central recirculation region. Due to the side flame's heat release the merging of primary and secondary flow is slightly shifted downwards [30]. It was argued by the authors, that the side flame exerts only a minor impact on the main flame's position. The main flame stabilizes by the mixing of hot centrally recirculated flue gasses with the rich mixture coming from the primary stream.

It can be estimated from Fig. 6 and the experimental data depicted further below that the side flame has a length of approximately 10 mm. Depending on the way the flame is ignited two different stable combustion modes develop. Applying a spacious ignition kernel a side flame formed in the simulation. However, this side flame was not only much larger than in the experiment but also merged with the main flame as it becomes clear from Fig. 7. In this depiction, mixture fraction and progress variable fields are given in gray scale for the same instantaneous snapshot, respectively. The colored lines indicate the chemical source term of CO2. The marks (**A**, **B**, **C**, etc.) represent different thermo-chemical states and are interpreted in manifold space in Fig. 8. **A** is the secondary stream consisting of pure air, whereas **B** denotes the rich primary stream. The lean and rich flammability limits are at $f_{\text{lean}} \approx 0.02$ and $f_{\text{rich}} \approx 0.1$, respectively, whereas stoichiometry is at around $f_{\text{stoich}} \approx 0.055$. Both, primary and secondary stream mix with each other. For a wide range of the mixing states between these two the mixture is inside the flammability limits. For this mixture fraction range, the start and progress of the chemical reaction is tabulated in

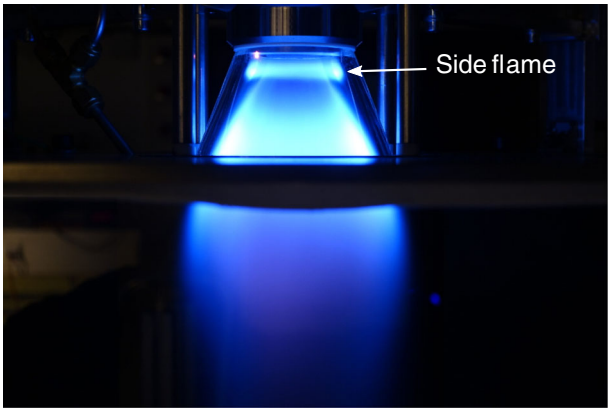

Fig. 6 Photography of the methane flame. Exposure time was set to 20 s for averaging the wrinkled flame front

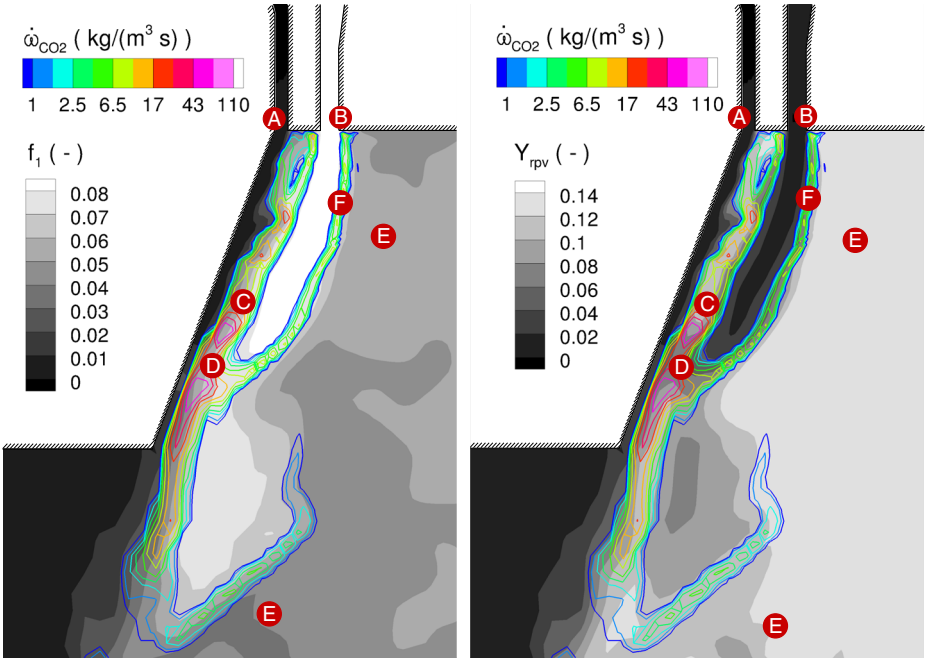

Fig. 7 Instantaneous contour of the operation mode with side flame in the quarl region. Left: mixture fraction. Right: reaction progress variable. The colored lines indicate the chemical source of CO2. The marks (**A**, **B**, **C**, etc.) represent different thermo-chemical states and are interpreted in manifold space in Fig. 8

the premixed flamelets based manifold. **C** is reached by this superposition of mixing and the proceeding of the reaction. The side flame thereby reveals a diffusion flame character since rich and lean mixtures are provided from opposing sides of the reaction zone. The numerical side flame is larger than in reality. In the following assumptions regarding the reason for this are made. A possible explanation is that the extinction process is triggered by the scalar dissipation rate present in the real shear and mixing layer between primary and secondary flow. In the simulation this side flame should be predicted by a manifold which is generated of premixed flamelets each featuring a scalar dissipation rate of zero that might lead to a significant overprediction in terms of size and intensity. Generally, the premixed manifold should be capable of describing this diffusion flame situation, particularly as even the rich flammability limit is not exceeded. However, it is also conceivable that the applied ATF model which maps the unresolved scales on the resolved LES grid impacts the extinction process of the side flame. Due to the thickening the time scales of extinction are also enlarged by the thickening factor which implies that the extinction process takes more time. Assuming an extinction strain rate in the order of $10^3\,\mathrm{s}^{-1}$ and a thickening factor of approximately 2 to 3 in the side flame region, one yields a representative extinction time of at least $2 \cdot 10^{-3}$ s. Considering the absolute value of the streamwise velocity component of up to 20 m/s extinction might not be completed before a path length of 40 mm which is almost the full quarl length. It seems that the side flame is sensitive to extinction processes since the flame's stable formation depends also on the operating point as it was shown by [30]. As a consequence of its larger extent the side flame merges with the main flame which encompasses the central recirculation zone. Here the reaction progress variable drops due

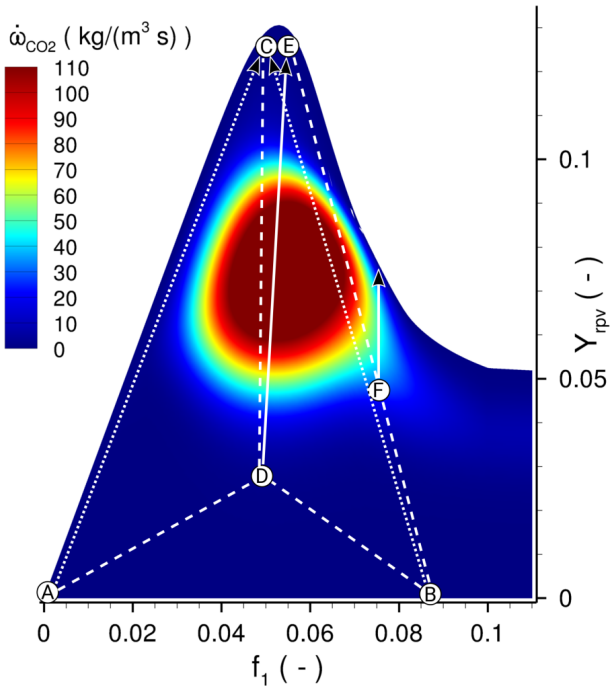

Fig. 8 Thermo-chemical states of the setting with side flames as indicated in Fig. 7. For simplicity a constant enthalpy level is depicted. Solid lines represent chemical reaction, whereas dashed lines illustrate mixing. Dotted lines indicate chemical reaction superimposed by mixing

to the rapid mixing of the remaining primary and secondary flow (**D**). This mixture then fully reacts at approximately stoichiometric conditions and forms the hot product gasses that partly recirculate in the core of the quarl **E**. They provide the activation energy for the main flame (**F**) that burns in a premixed mode. Due to the significant misprediction of the side flame reaction, the flow field inside the quarl is strongly affected so that a sufficient agreement with experimental data could not be obtained.

If a more compact ignition kernel is used for igniting the flame, there is no provision of activation energy in the region between primary and secondary stream nozzles so that no side flame developed in the simulation. At this operating mode only a main flame forms which is depicted in Fig. 9. Hence, the stable combustion mode depends on the initial conditions which is plausible. It cannot be replicated anymore how the ignition procedure was conducted in the experiment so that an uncertainty remains in this regard. The fact that the side flame – if existing – cannot be predicted correctly can be attributed to modeling shortcomings mentioned above.

Analogously to the analysis above, the corresponding thermo-chemical states are interpreted in manifold space for the mode without side flame in Fig. 10. Here, **A** and **B** are still the secondary and primary stream consisting of pure air and a rich but flammable mixture, respectively. In this mode these flows directly mix after leaving their nozzles. Depending on the mixing distance different states being either rich (**C"**), stoichiometric (**C**) or lean (**C'**) are gained whereby mixing is facilitated by the turbulent motions. These states then

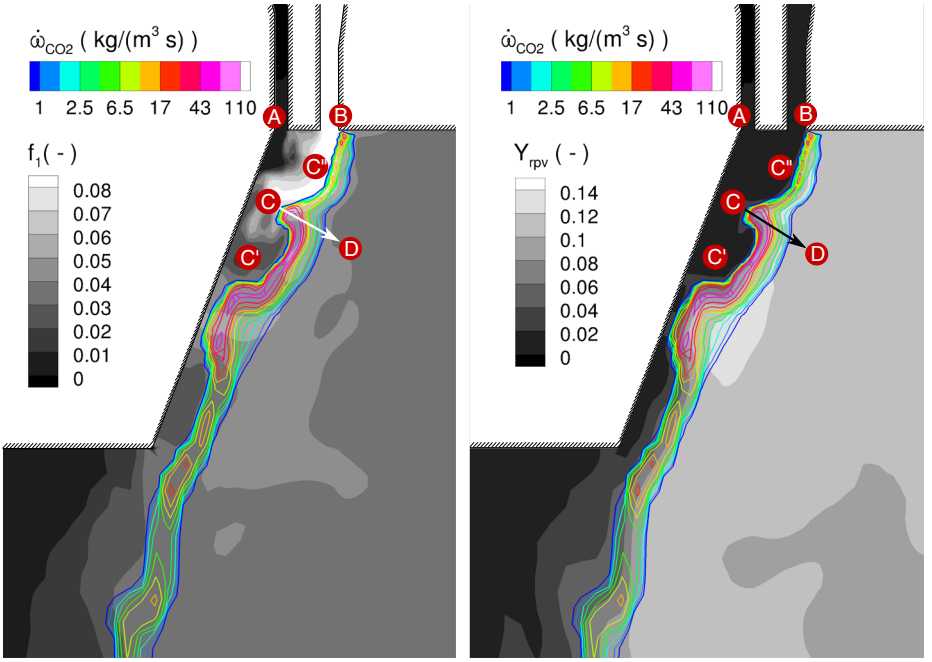

Fig. 9 Instantaneous contour of the setting without side flames in the quarl region. Left: mixture fraction. Right: reaction progress variable. The colored lines indicate the chemical source of CO2. The marks (**A**, **B**, **C**, etc.) represent different thermo-chemical states and are interpreted in manifold space in Fig. 10

react with the hot recirculated product gasses (**D**) in a predominantly premixed and stratified mode. This reaction is exemplarily illustrated with the arrow in Figs. 9 and 10. As it was also pointed out by Becker et al. [30] the main flame reveals a premixed character at medium and large distances from the nozzle where primary and secondary stream have sufficiently mixed. Also because of this finding, the latter discussed operating mode without side flame is far closer to the experimentally investigated case. Hence, it will be taken in the following. The absence of the side flame does not constitute a hard constraint as it has only a minor impact on the field inside the quarl [30].

In Figs. 11 and 12 the velocity components of the single-phase reactive operating point inside and below the quarl are depicted for different heights. It should be mentioned that experimental data are not available for heights above $z \approx 30$ mm in the wall near region. Since in the numerical simulation the side flame did not form and primary and secondary flow mix with each other, this zone is of particular interest. It was stated in [30] that intense reflections prohibited the processing of the velocity field in this region. Inside the quarl, the velocity fields of the non-reactive case and this reactive setup are similar. Differences occur below the quarl where larger velocity magnitudes are observed for the reactive case. They are a consequence of the heat release. Since the latter evokes changes in the density and hence, the velocity field, the good agreement between numerical and experimental results indicates that the chemical reaction is overall well reproduced by the simulation. However, it can be seen from the axial velocity component in the lower heights of the quarl that the layer near the wall appears slightly thicker in the numerical simulation. It can be deduced from the corresponding data plotted in Fig. 12 that the experimental configuration was not

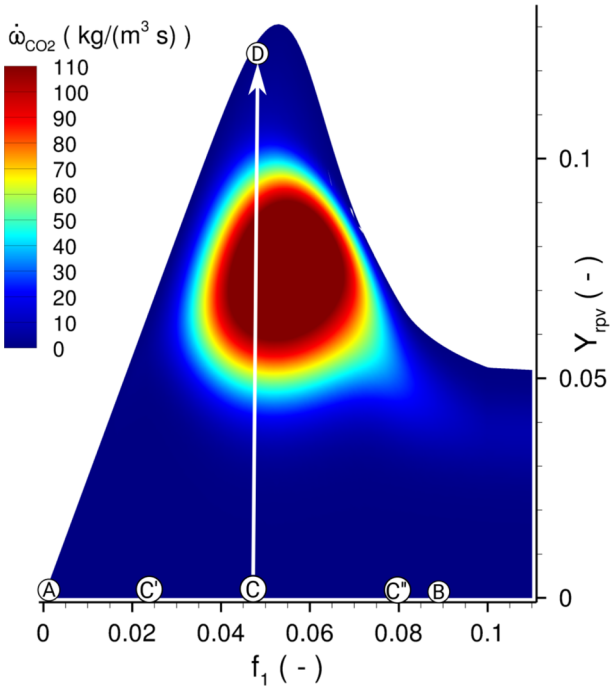

Fig. 10 Thermo-chemical states of the operation mode without side flame as indicated in Fig. 9. For simplicity a constant enthalpy level is depicted.

fully symmetric which was also reported in [30]. Keeping that in mind agreement was good also in the non-confined region below the quarl. Concluding from that it seems that the side flame present in reality does not have a large impact on the flow field. Hence, its heat release and the consequential density change appears to be small. The negligence of the side flame was therefore considered reasonable. Becker et al. [30] also argue that the side flame hardly affects the main flame's position.

The following illustrations allow for an impression of the reaction zone. In Figs. 13 and 14 numerically obtained mean OH mass fraction fields inside and below the quarl are compared with the mean OH fluorescence signal from the experiment. Since the experimental field inside the quarl was almost symmetric the depiction (Fig. 13) was split in the middle. This was not the case below the quarl. Hence, an unseparated representation is shown in Fig. 14. The figures provide information about the spatial extent of the chemical reaction. It becomes clear in the comparison that the side flame was not ignited in the numerical simulation. Apart from that the OH mass fraction of the main flame is very similar to the corresponding fluorescence signal. This also indicates that the side flame is of minor relevance for the overall combustion inside the quarl. In principle a comparable situation turns out to be present below the quarl. The OH indicating the reaction zone as well as hot gas zones has a very similar radial extent. However, it appears to be somewhat longer and comprises the internal recirculation zone more in the experiment. By judging from that it should be kept in mind that the OH fluorescence counts constitute a non-quantitative signal which is not identical to the OH mass fraction.

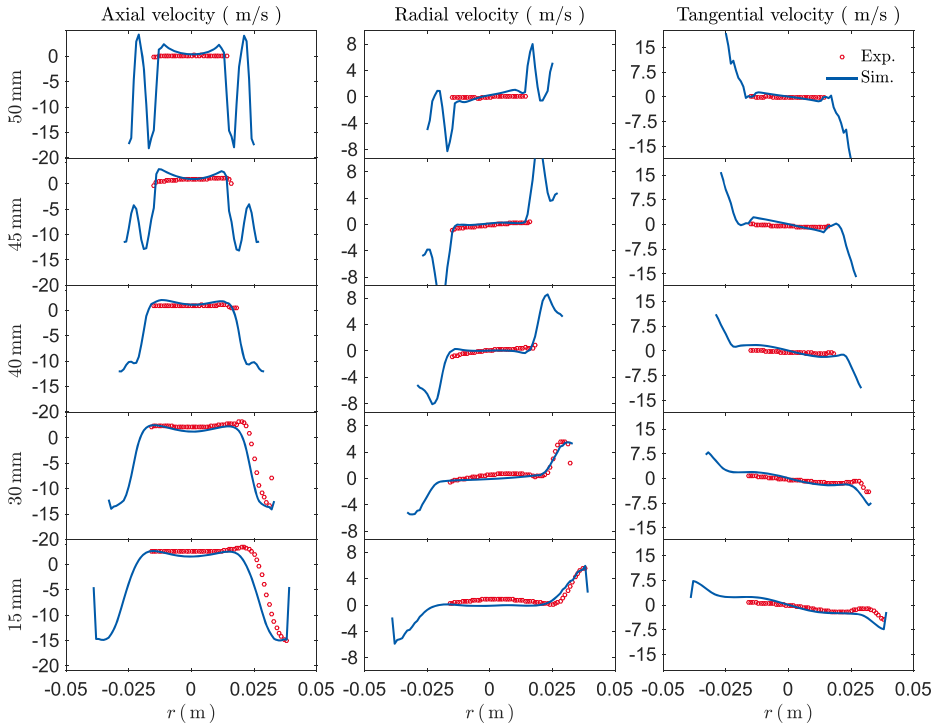

Fig. 11 Comparison of single-phase reactive experimental and numerical mean velocity data inside the quarl for different heights

In the analysis of the experimental data the flame brush was determined [30]. For this, the canny edge filter was applied to instantaneous OH images in order to identify strong spatial gradients that correlate with the reaction front and hence, separate cold and hot gasses. The flame brush then represents a spatial probability density function of this edge's position for a sufficiently large number of instants. Primarily, the flame brush is an information about the flame's position.

It was also determined from the numerical data. A comparison is depicted in Figs. 15 and 16. Apart from the absent side flame good agreement between experiment and simulation is shown in Fig. 15. As it can be seen from the narrow flame brush close to the nozzle, the reaction zone of the main flame is thin and smooth. It becomes wider and wrinkled in the lower half of the quarl. These essential characteristics including the spreading and the brush's inclination angle are well reproduced by the numerical simulation. However, it appears that the numerical brush is somewhat closer to the quarl's wall than the experimental brush. This is likely due to the missing heat release of the side flame. As already argued before there was no laser excitation inside the quarl below $z \approx 9\,\mathrm{mm}$ and hence, no signal. Below the quarl (Fig. 16) the experimental brush features an almost symmetric shape despite the more asymmetric OH fluorescence given in Fig. 14. This illustrates that a signal's strength becomes less decisive than its gradient's position when binarized. It can also be seen that both brushes feature a similar shape in terms of length, global widening and thickness.

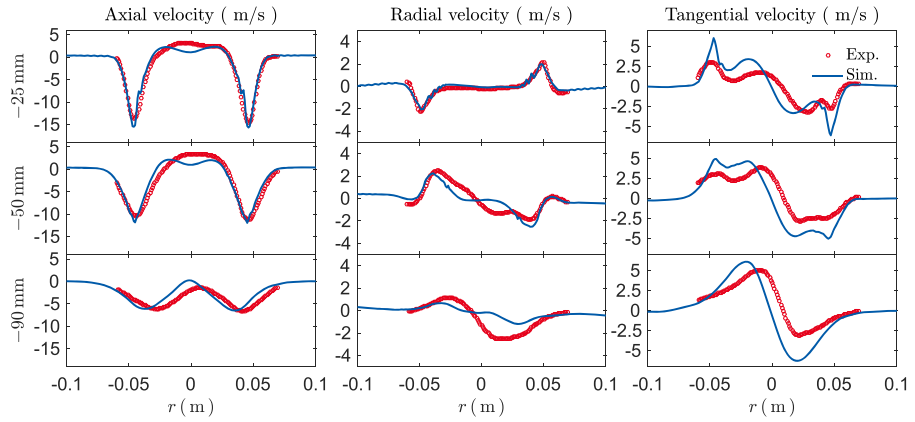

Fig. 12 Comparison of single-phase reactive experimental and numerical mean velocity data below the quarl for different heights

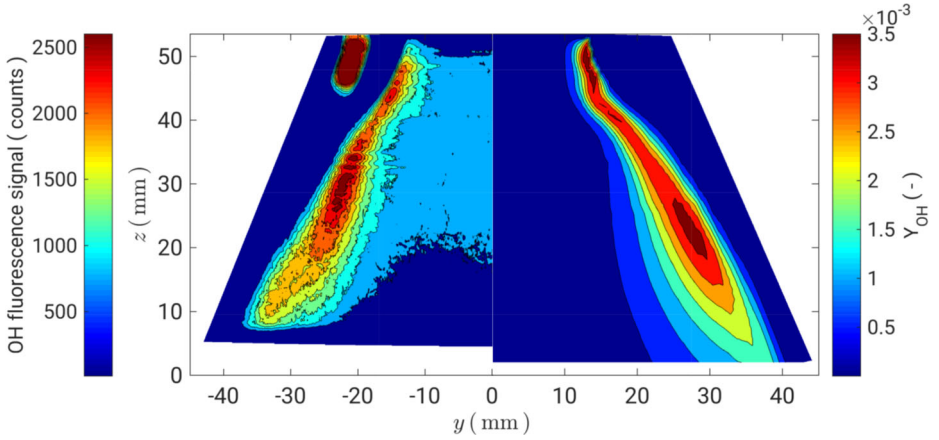

Fig. 13 Results for OH inside the quarl. Left half: Experimentally obtained mean OH fluorescence signal. The fluorescence signal vanishes below $z \approx 9\,\text{mm}$ since there was no laser excitation in this region. Right half: Mean OH mass fraction field obtained by numerical simulation

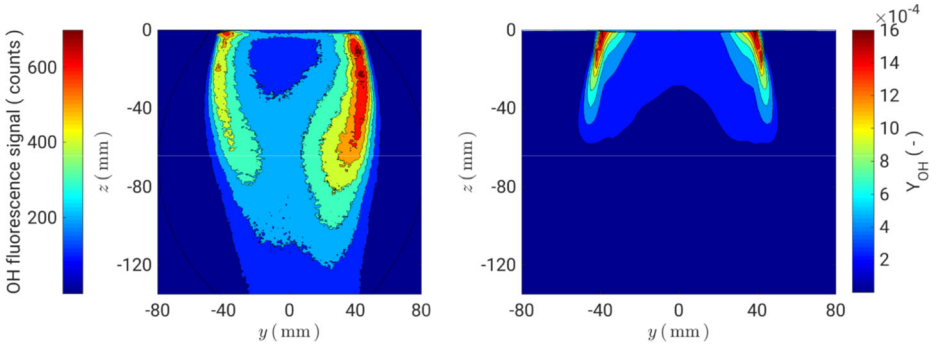

Fig. 14 Results for OH below the quarl. Left: Experimentally obtained mean OH fluorescence signal. Right: Mean OH mass fraction field obtained by numerical simulation

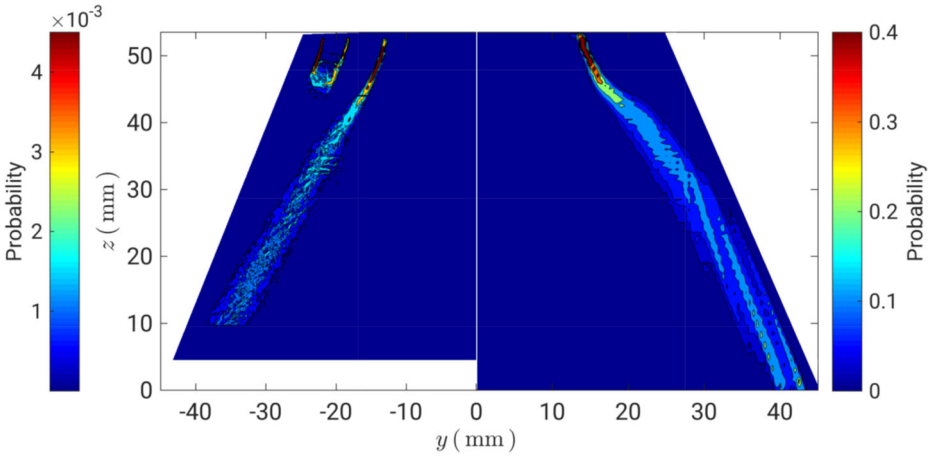

Fig. 15 Experimentally (left) and numerically (right) obtained flame brush inside the quarl

In summary, the formation of a side flame in the numerical simulation depended on the ignition region. It was shown that the former could not be sufficiently predicted with the applied modeling approach based on premixed flamelets. Without side flame a reaction zone formed which was in better accordance with experimental findings. Good agreement with experimental data in terms of velocity field as well as shape and position of this main reaction zone could be obtained in this regard. Due to the main flame's premixed character the choice of a premixed flamelet database appears to be appropriate. The absence of the side flame did not constitute an issue in terms of overall predictability.

4.3 Two-phase reactive

On the basis of the above discussed findings it was decided to take the operating mode without side flame as the gas flame that supports the coal combustion in the TPR setup as specified in Table 3. Coal particles having the size distribution as given in Fig. 3 and the properties specified in Table 4 were additionally injected in the primary stream. A total of 2.1 s was simulated which yielded sufficiently converged statistics for both, gaseous and particle phase. In this section, emphasis is put on the particle phase, the coal conversion inside the chamber and the particle's impact onto the gas phase combustion. In terms of

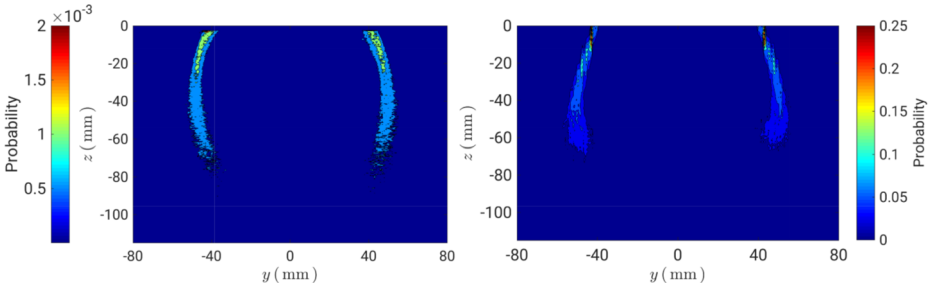

Fig. 16 Experimentally (left) and numerically (right) obtained flame brush below the quarl

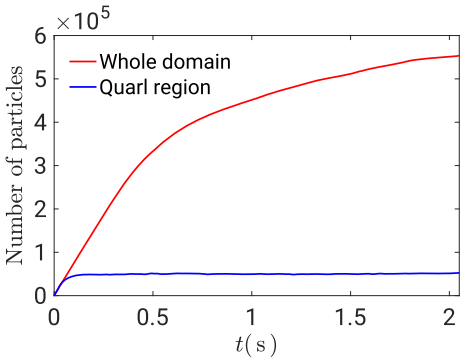

Fig. 17 Number of particles in the whole combustion chamber and the quarl region, respectively. The latter is defined as the quarl itself and the cylindrical zone with a radius of 80 mm and a length of 200 mm directly below the quarl

available experimental data only gas phase velocity fields of the two-phase reactive flow can be taken for comparison. The chemical reaction at this operating point must be analyzed solely on the basis of numerical results.

In Fig. 17 the number of particles inside the whole combustion chamber and the quarl region, respectively, is depicted. It can be observed that it takes approximately 0.1 s after the start of injection until the particles have accumulated to a statistically stationary number inside the quarl region which is driven by the recirculation zone. Considering the whole chamber the convergence against a steady state takes significantly longer due to the larger volume and the correspondingly larger residence times. In the following, the evaluation of particle statistics was started when the particle number had converged a stationary value in the region of interest.

In Fig. 18 particle histories with regards to the particle temperature and the particle volatiles mass fraction are depicted. In order to differentiate with respect to the particle size, particles are assigned to different classes which are specified in Table 5.

In each class thousand different particles were evaluated which is a statistically sufficient large number. As expected the smaller particles are exposed to a more rapid heat up than the larger ones. However, it appears as if class 2 particles exhibit a slightly steeper temperature increase than the smaller ones in class 1. Furthermore, the variation of particle histories is stronger for class 1 particles during heat up. This behavior can likely be attributed to the smaller Stokes number of class 1 particles which enable them to better follow the turbulent motions after leaving the primary stream nozzle. On the one hand, the turbulence increases the variance. On the other hand, class 1 particles better follow the primary flow which is deflected to the wall of the quarl, whereas class 2 particles are rather carried into the reaction zone directly which is due to their different particle dynamics. Apart from particles belonging to class 5, the maximum T_{prt} values reached at the end of particle heat up do not strongly correlate with the particle size. With regard to the devolatilization dynamics it can be observed that the volatiles of most of the particles have already been fully released to the gas phase after 0.05 s. The largest ones being assigned to class 5 require approximately 0.2 s which is mainly due to their larger thermal inertia.

Analogously to Fig. 18, the ambient conditions the particles encounter are depicted in Fig. 19. It is noticeable that class 1 particles being the lightest experience a less steep gradient in terms of Y_{CO2} and T. Hence, they enter the hot product gasses in the inner core of the quarl somewhat slower than the heavier particles which is likely due to their different particle dynamics. They better follow the turbulent swirling motion and are therefore rather deflected toward the wall near velocity layer whereas the chemical reaction takes place at

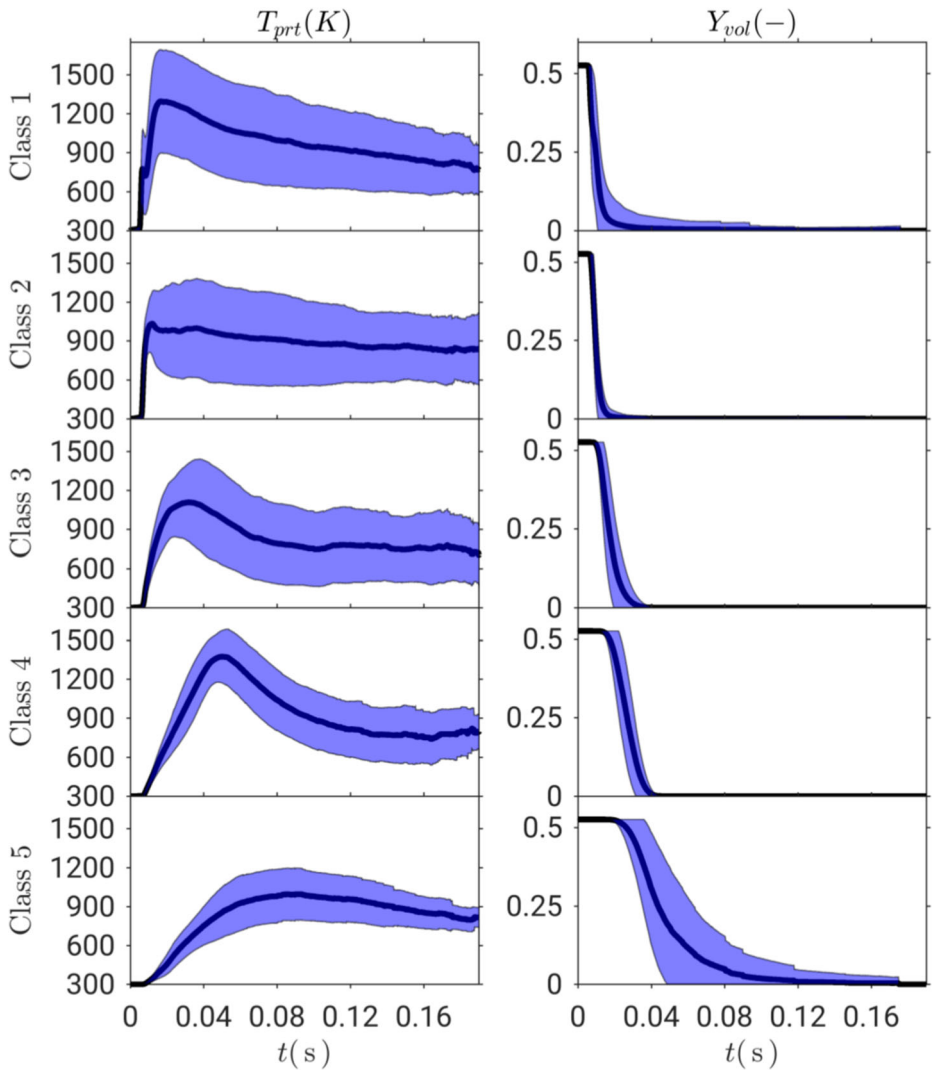

Fig. 18 Particle histories with regards to particle temperature and particle volatiles mass fraction. The classes are specified in Table 5. The black lines indicate the mean values. The variation represented by one standard deviation is depicted by the blue areas. The time line in this figure starts at a statistically stationary point

smaller radii. Larger particles tend to leave the nozzle in a more direct way leading to a more rapid exposure to product gasses. It can also be seen from the f_1-histories that the heavier particles are exposed slightly longer to the richer conditions close to the nozzle.

Concluding from Fig. 18 all particles are subject of cooling down that starts directly after heat up. The particle temperature decrease is weaker than the changing rate during heat up. Slight deviations occur between the classes. They are probably driven by the particle dynamics. Depending on their Stokes number particles are carried into combustion chamber zones with different temperature levels.

Table 5 Partition of particles into different classes according to their size for post-processing

Class	Particle size
1	$D_{\text{prt}} \leq 10\,\mu\text{m}$
2	$10\,\mu\text{m} < D_{\text{prt}} \leq 25\,\mu\text{m}$
3	$25\,\mu\text{m} < D_{\text{prt}} \leq 60\,\mu\text{m}$
4	$60\,\mu\text{m} < D_{\text{prt}} \leq 100\,\mu\text{m}$
5	$D_{\text{prt}} > 100\,\mu\text{m}$

The temporally averaged gas phase temperature of the combustion chamber's upper half is given in Fig. 20 both, for the SPR and the TPR case. First, because of the reaction of the additionally injected coal particles the hot temperature region is extended downwards and also slightly in radial direction. Second, a medium temperature range has formed right below the bluff body on the center axis in the TPR case. As it will also be shown below, this is likely due to the fact that a richer mixture forms inside the quarl as a consequence of the volatiles release which spatially shifts the region of chemical reaction. However, the extent of the spatial range featuring a temperature level which is sufficiently large to induce the reaction of coal particles is limited to the inner core of the chamber. Significant conversion of char requires large residence times in hot combustion chamber regions. At larger radii the gas phase temperature is quite low contributing to a char conversion process that takes place only to a minor amount in this configuration. In Fig. 21 a histogram of the particle

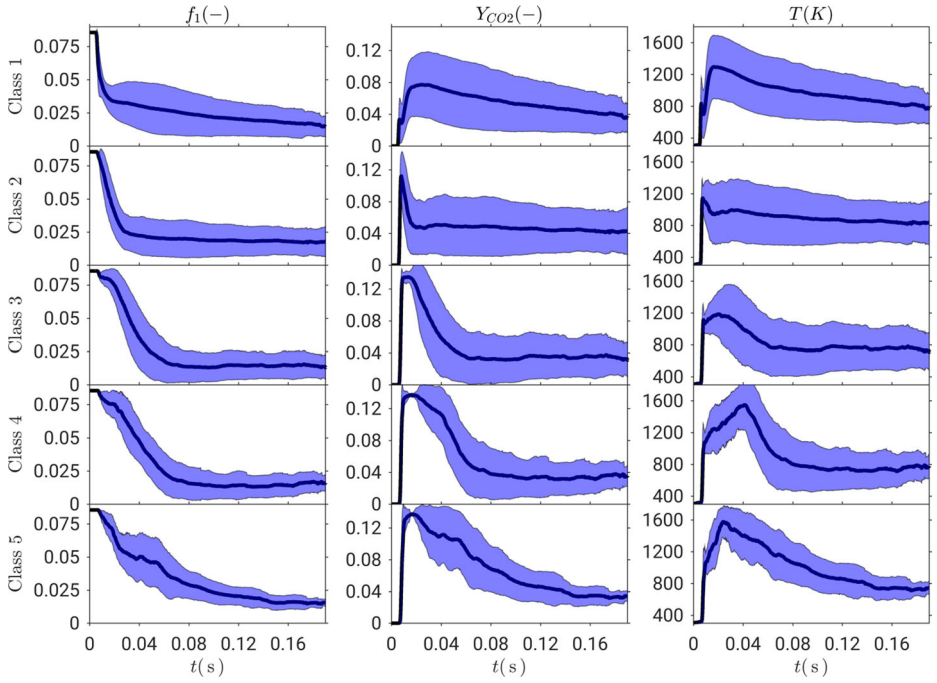

Fig. 19 Ambient conditions the particles are exposed to on their path with regards to first mixture fraction, mass fraction of CO2 and gas phase temperature. The classes are specified in Table 5. The black lines indicate the mean values. The variation represented by one standard deviation is depicted by the blue areas. The time line in this figure starts at a statistically stationary point

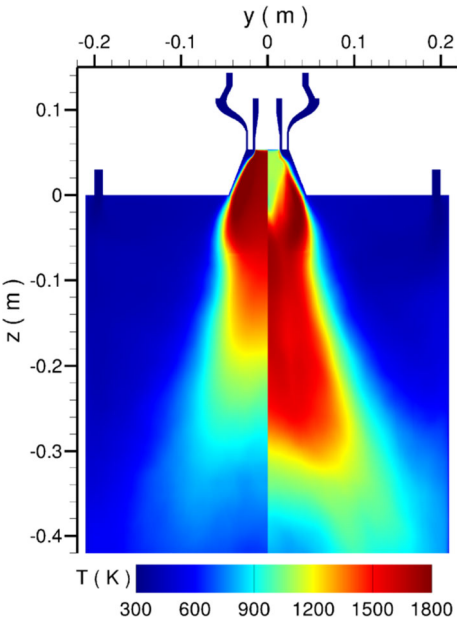

Fig. 20 Temporally averaged gas phase temperature field in mid section plane. Left: single-phase reactive. Right: two-phase reactive

char mass fraction considering all particles in the chamber is depicted. The particles' initial char mass fraction is given in Table 4. It can be seen that only a minor portion of all particles has converted to a marginal degree. These findings are in agreement with the low numerical values of the second mixture fraction (Fig. 22) which represents the mass fraction of gaseous char conversion products. For instance, in semi-industrial coal furnaces the mass fraction of char products is approximately two orders of magnitude larger [12, 13]. Generally, f_2 strongly correlates with the gas phase temperature field (Fig. 20) which is plausible as the slow char conversion process requires rather high temperatures. It can be concluded that char burnout does not play a significant role in this configuration.

As it was shown in Fig. 18 devolatilization is completed after approximately 0.2 s for almost all particles. The release of the volatiles mass affects the first mixture fraction as it is demonstrated for the quarl region in Fig. 23. As expected, the volatiles release leads to a significantly richer mixing field which is partly very close or even slightly beyond the rich flammability limit $f_{\text{rich}} \approx 0.1$. The richest region has formed right below the bluff body

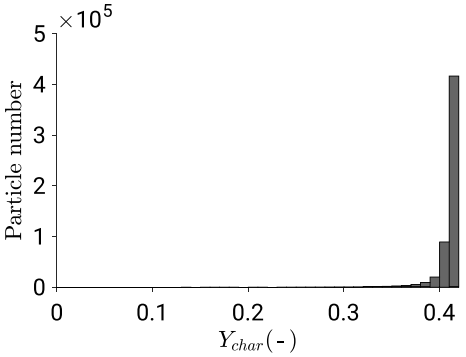

Fig. 21 Particle histogram with regards to particle char mass fraction at $t = 2.06$ s according to the time line in Fig. 17

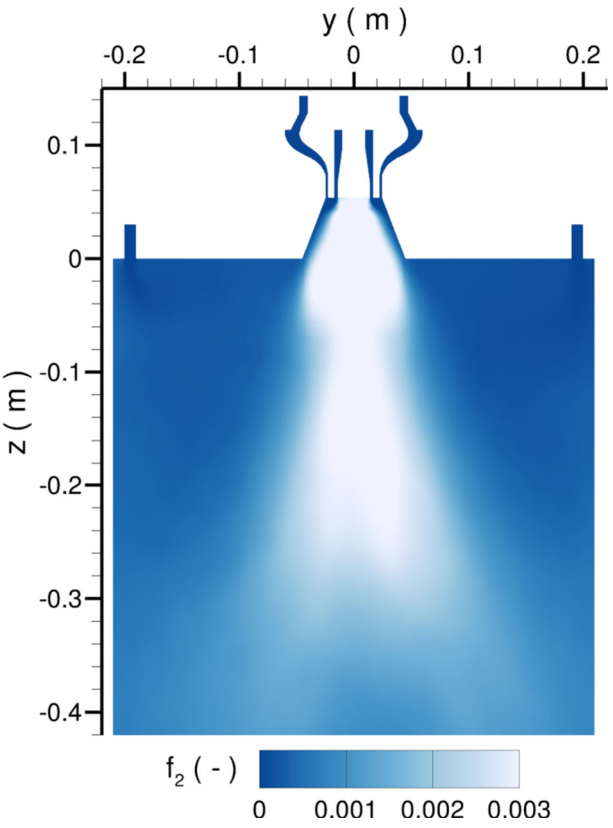

Fig. 22 Temporally averaged field of the second mixture fraction in mid section plane

in the proximity of the recirculation zone's stagnation point. Due to the reduced chemical reactivity a temperature decrease could be observed as it is depicted in Fig. 20. In comparison to the single-phase reactive operating point SPR, position and strength of the reaction zone are influenced by the mixing field. As it is shown in Fig. 24 the reaction is shifted more downstream and appears to be rather distributed, which is a consequence of the following mechanism: As it can be seen in Fig. 23, the release of volatile matter in the quarl region results in significantly richer conditions beyond the stoichiometric point. Correspondingly, compared to the single-phase reactive case Figs. 24 and 20 depict, that the two-phase flow is characterized by lower reaction rates and resulting temperatures in the quarl, respectively. However, an enhancement of the chemical reaction with increasing distance from the quarl becomes obvious and can be attributed to the coal particles. Due to continuous mixing with oxygen and devolatilization, the hot temperature region considerably enlarges, which represents the contribution of the thermal power of the coal. At this point it should be noted that the assumption of the volatiles solely consisting of methane affects the stoichiometry in comparison to a more realistic composition. For instance, the oxygen amount available in the quarl region would probably be somewhat larger than it is the case with the applied modeling approach. This could result in an increased char reactivity. However, the latter effect is not expected to be substantially large, since it appears from the strong correlation between the gas phase temperature and the f_2-field that the gas phase temperature is the

more important driving force of the char conversion in this configuration than the available oxygen amount. This indication also appears to be plausible as the char conversion is restricted to the hot regions, although sufficient oxygen amounts are provided by the tertiary stream. In the model formulation the larger standard formation enthalpy of methane compared to realistic volatiles is considered by a corresponding sink term in the enthalpy equation. This way, it is ensured that the methane volatiles feature the same adiabatic flame temperature as a realistic composition. Hence, the gas phase temperature field should not be affected by the volatiles composition assumption. In terms of combustion modeling, the applied premixed flamelet approach seems to be appropriate. First, the assisting methane flame has a premixed character. Second, volatiles release mainly takes place in the quarl region which can be deduced from Fig. 23. A rather homogeneous mixture forms in this region implying low scalar dissipation rates. Hence, the chemical states are appropriately describable by a premixed approach.

In Figs. 25 and 26 experimentally and numerically obtained gas phase velocity data are compared with each other. Due to the PIV setup the tangential velocity being the out-of-plane component could not be detected. Both, inside and below the quarl there is an overall good agreement with respect to the axial velocity component. Right below the nozzle where the particles have just exited the primary flow channel the particle number density is quite high which constitutes a challenge for the post-processing algorithm. In this high particle number density region the systematic measurement error is larger than in other regions. Therefore, discrepancies between experimental and numerical results should not be overrated. In terms of the radial component peak velocity values are approximately met.

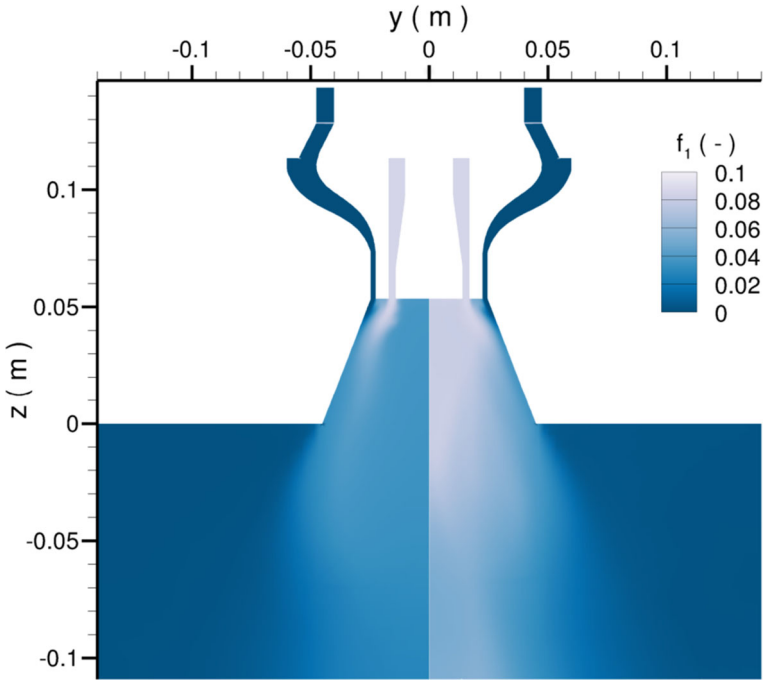

Fig. 23 Temporally averaged fields of the first mixture fraction. Left half: single-phase reactive operating point. Right half: two-phase reactive operating point

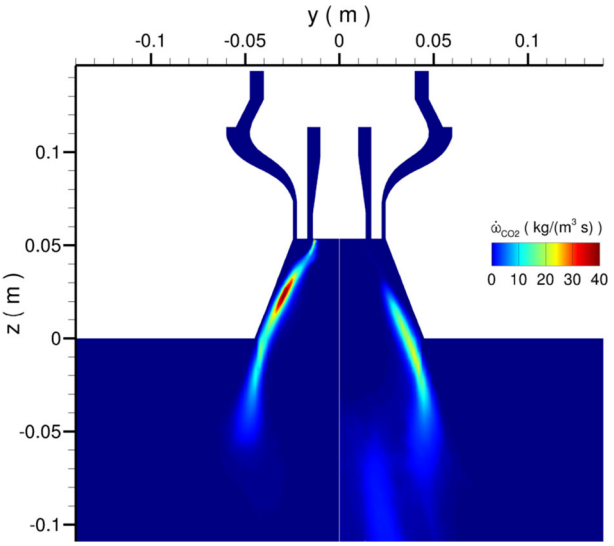

Fig. 24 Temporally averaged fields of the chemical source term of CO2. Left half: single-phase reactive operating point. Right half: two-phase reactive operating point

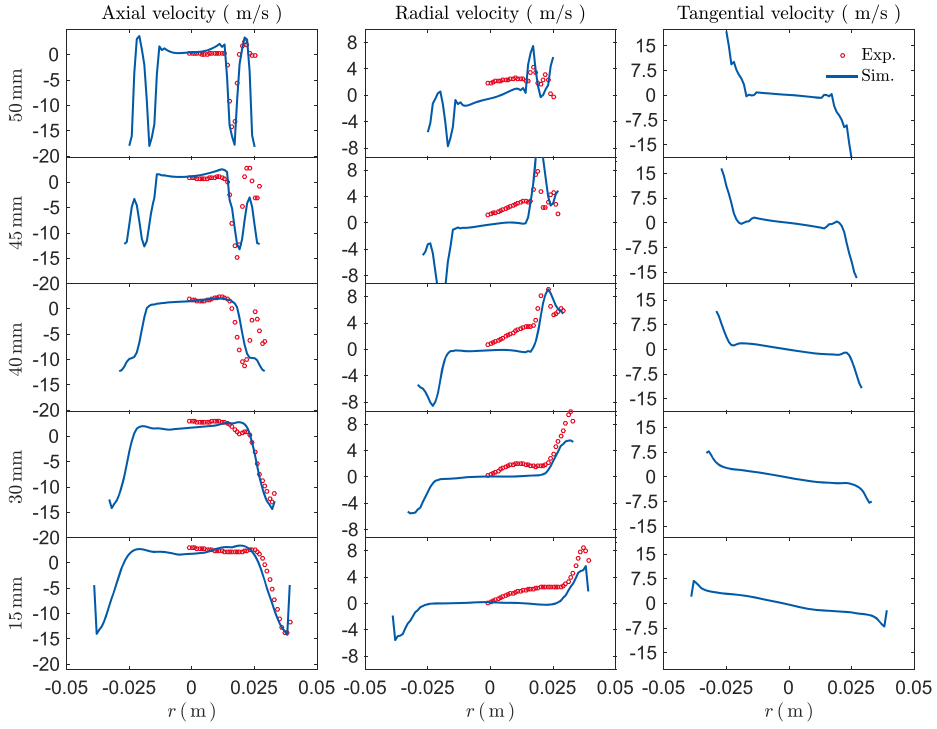

Fig. 25 Comparison of two-phase reactive experimental and numerical mean gas phase velocity data inside the quarl for different heights

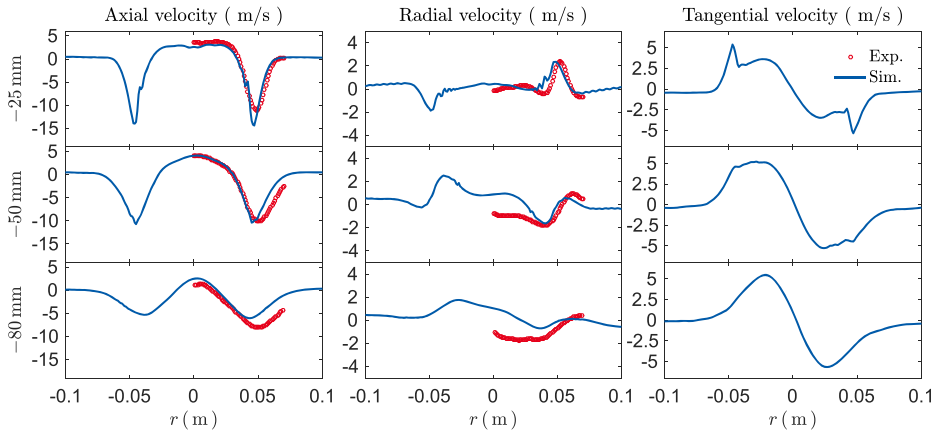

Fig. 26 Comparison of two-phase reactive experimental and numerical mean gas phase velocity data below the quarl for different heights

However, slight deviations in a low velocity range occur. Their reason must also be evaluated in an analysis of the measurement technique's error which would be beyond the scope of this work. In summary, it can be concluded that essential characteristics of the velocity field are well reproduced.

5 Summary and Conclusion

A four-dimensional FGM modeling approach was applied in a first reactive LES of a laboratory scale coal combustion chamber in which a methane flame assists and stabilizes the combustion of coal particles [30]. Different operating points with successively increased complexity were investigated. These are single-phase non-reactive, single-phase reactive and two-phase reactive flows. Due to the good optical accessibility, experimental data arising from laser diagnostics measurements were available for comparison with the numerical results. Good agreement regarding the velocity field of the single-phase non-reactive field was found. In terms of the reactive operating points a main flame forms within the burner quarl that encompasses the internal reaction zone. Depending on the ignition procedure a side flame next to this main flame exists. In reality this side flame has only a marginal impact on the flow field inside the burner quarl. It was found that the applied modeling approach could well reproduce both, the characteristics of the reaction zone and the velocity field of the stable combustion mode featuring no side flame. In terms of the two-phase reactive operating point, coal particles were additionally injected. They nominally provided the same thermal power (20 kW) as the assisting methane flame. An analysis of particle histories revealed a rapid heat up that induced devolatilization. Depending on the particle size slight differences were observed with respect to particle heating rates and maximum particle temperature. These can be attributed on the one hand to the different thermal inertia but on the other also to the different Stokes number that affects the particle path within the turbulent flow. Devolatilization of almost all particles was completed after approximately 0.2 s. In this phase particles have already left the hot zones so that their temperature reduces again. Due to the short residence times of particles within high temperature regions only a small fraction of char conversion evolves within the chamber. The mass fraction of gaseous char

burnout products is on a low level and strongly correlates with the gas phase temperature field. As a consequence of particle devolatilization the near quarl region in which gas phase combustion is stabilized becomes richer. This leads to lower chemical reaction rates inside the quarl. However, the reaction is enhanced with increasing distance to the quarl compared to the single-phase reactive case, which is due to continuous mixing with oxygen and devolatilization. As a consequence, the hot temperature region is significantly enlarged. In terms of the gas phase velocity field, good agreement to experimental data could be obtained with respect to essential flow characteristics in general and the axial component in particular. Overall, insights into different aspects of the coal combustion process could be gained. Mainly, an understanding of the physical processes within the chamber was obtained. Furthermore, it was found that the applied model was capable of reproducing these processes to a good degree.

Acknowledgements The authors kindly acknowledge financial support through Deutsche Forschungsgemeinschaft (DFG) through SFB/TRR 129. Computations were performed on the Lichtenberg High Performance Computer in Darmstadt.

Funding Information This study was funded by Deutsche Forschungsgemeinschaft (SFB/TRR 129).

Conflict of interests The authors declare that they have no conflict of interest.

References

1. International Energy Agency: Key World Energy Statistics 2016 (2016)
2. Hwang, S.M., Kurose, R., Akamatsu, F., Tsuji, H., Makino, H., Katsuki, M.: Application of optical diagnostics techniques to a Laboratory-Scale turbulent pulverized coal flame. Energy Fuels **19**, 382–392 (2005)
3. Franchetti, B.M., Cavallo Marincola, F., Navarro-Martinez, S., kempf, A.M.: Large Eddy simulation of a pulverised coal jet flame. Proc. Combust. Inst. **34**, 2419–2426 (2013)
4. Kurose, R., Makino, H.: Large eddy simulation of a solid-fuel jet flame. Combust. Flame **135**, 1–16 (2003)
5. Wen, X., Jin, H., Stein, O.T., Fan, J., Luo, K.: Large Eddy Simulation of piloted pulverized coal combustion using the velocity-scalar joint filtered density function model. Fuel **158**, 494–502 (2015)
6. Zhao, X.Y., Haworth, D.C.: Transported PDF modeling of pulverized coal jet flames. Combust. Flame **161**(7), 1866–1882 (2014)
7. Stein, O.T., Olenik, G., Kronenburg, A., Cavallo Marincola, F., franchetti, B.M., Kempf, A.M., Ghiani, M., Vascellari, M., Hasse, C.: Towards Comprehensive Coal Combustion Modelling for LES. Flow Turbul. Combust. **90**, 859–884 (2013)
8. Rieth, M., Clements, A.G., Rabaçal, M., Proch, F., Stein, O.T., Kempf, A.M.: Flamelet LES modeling of coal combustion with detailed devolatilization by directly coupled CPD. Proc. Combust. Inst. **36**(2), 2181–2189 (2017)
9. Hara, T., Muto, M., Kitano, T., Kurose, R., Komori, S.: Direct numerical simulation of a pulverized coal jet flame employing a global volatile matter reaction scheme based on detailed reaction mechanism. Combust. Flame **162**(12), 4391–4407 (2015)
10. Olenik, G., Stein, O.T., Kronenburg, A.: LES Of swirl-stabilised pulverised coal combustion in IFRF furnace No. 1. Proc. Combust. Inst. **35**, 2819–2828 (2015)
11. Rabaçal, M., Franchetti, B.M., Cavallo Marincola, F., Proch, F., Costa, M., Hasse, C., Kempf, A.M.: Large Eddy Simulation of coal combustion in a large-scale laboratory furnace. Proc. Combust. Inst. **35**, 3609–3617 (2015)

12. Rieth, M., Proch, F., Clements, A.G., Rabaçal, M., Kempf, A.M.: Highly resolved flamelet LES of a semi-industrial scale coal furnace. Proc. Combust. Inst. **36**(3), 3371–3379 (2017)
13. Rieth, M., Proch, F., Rabaçal, M., Franchetti, B.M., Marincola, F.C., Kempf, A.M.: Flamelet LES of a semi-industrial pulverized coal furnace. Combust. Flame **173**, 39–56 (2016)
14. Watanabe, J., Yamamoto, K.: Flamelet model for pulverized coal combustion. Proc. Combust. Inst. **35**, 2315–2322 (2015)
15. Watanabe, J., Okazaki, T., Yamamoto, K., Kuramashi, K., Baba, A.: Large-eddy simulation of pulverized coal combustion using flamelet model. Proc. Combust. Inst. **36**(2), 2155–2163 (2017)
16. Wen, X., Luo, K., Jin, H., Fan, J.: Numerical investigation of coal flamelet characteristics in a laminar counterflow with detailed chemistry. Fuel **195**, 232–242 (2017)
17. Wen, X., Luo, K., Wang, H., Luo, Y., Fan, J.: Analysis of pulverized coal flame stabilized in a 3D laminar counterflow. Combust. Flame **189**, 106–125 (2018)
18. Wen, X., Luo, Y., Luo, K., Jin, H., Fan, J.: LES Of pulverized coal combustion with a multi-regime flamelet model. Fuel **188**, 661–671 (2017)
19. Wen, X., Wang, H., Luo, Y., Luo, K., Fan, J.: Evaluation of flamelet/progress variable model for laminar pulverized coal combustion, vol. 29 (2017)
20. Messig, D., Vascellari, M., Hasse, C.: Flame structure analysis and flamelet progress variable modelling of strained coal flames. Combust. Theory Modell. **21**, 1–22 (2017)
21. Vascellari, M., Tufano, G.L., Stein, O.T., Kronenburg, A., Kempf, A.M., Scholtissek, A., Hasse, C.: A flamelet/progress variable approach for modeling coal particle ignition. Fuel **201**, 29–38 (2017)
22. Vascellari, M., Xu, H., Hasse, C.: Flamelet modeling of coal particle ignition. Proc. Combust. Inst. **34**, 2445–2452 (2013)
23. Xu, H., Hunger, F., Vascellari, M., Hasse, C.: A consistent flamelet formulation for a reacting char particle considering curvature effects. Combust. Flame **160**(11), 2540–2558 (2013)
24. Habermehl, M., Erfurth, J., Toporov, D., Förster, M., Kneer, R.: Experimental and numerical investigations on a swirl oxycoal flame. Appl. Therm. Eng. **49**, 161–169 (2012)
25. Habermehl, M., Hees, J., Massmeyer, A., Zabrodiec, D., Hatzfeld, O., Kneer, R.: Comparison of flame stability under air and Oxy-Fuel conditions for an aerodynamically stabilized pulverized coal swirl flame. J. Energy Resour. Technol. **138**(4), 042,209 (2016)
26. Hees, J., Zabrodiec, D., Massmeyer, A., Habermehl, M., Kneer, R.: Experimental Investigation and Comparison of Pulverized Coal Combustion in CO_2/O_2 and N_2/O_2 Atmospheres. Flow Turbul. Combust. **96**, 417–431 (2016)
27. Heil, P., Toporov, D., Stadler, H., Tschunko, S., Förster, M., Kneer, R.: Development of an oxycoal swirl burner operating at low O_2 concentrations. Fuel **88**, 1269–1274 (2009)
28. Toporov, D., Bocian, P., Heil, P., Kellermann, A., Stadler, H., Tschunko, S., Förster, M., Kneer, R.: Detailed investigation of a pulverized fuel swirl flame in CO2/O2 atmosphere. Combust. Flame **155**, 605–618 (2008)
29. Zabrodiec, D., Hees, J., Massmeyer, A., vom Lehn, F., Habermehl, M., Hatzfeld, O., Kneer, R.: Experimental investigation of pulverized coal flames in CO_2/O_2- and N_2/O_2-atmospheres: Comparison of solid particle radiative characteristics. Fuel **201**, 136–147 (2017)
30. Becker, L.G., Kosaka, H., Böhm, B., Doost, S., Knappstein, R., Habermehl, M., Kneer, R., Janicka, J., Dreizler, A.: Experimental investigation of flame stabilization inside the quarl of an oxyfuel swirl burner. Fuel **201**, 124–135 (2017)
31. Doost, A., Ries, F., Becker, L., Bürkle, S., Wagner, S., Ebert, V., Dreizler, A., di Mare, F., Sadiki, A., Janicka, J.: Residence time calculations for complex swirling flow in a combustion chamber using large-eddy simulations. Chem. Eng. Sci. **156**, 97–114 (2016)
32. Knappstein, R., Kuenne, G., Meier, T., Sadiki, A., Janicka, J.: Evaluation of coal particles volatiles reaction by using detailed kinetics and FGM tabulated chemistry. Fuel **201**, 39–52 (2017)
33. Lehnhäuser, T., Schäfer, M.: Improved linear interpolation practice for finite-volume schemes on complex grids. Int. J. Numer. Methods Fluids **38**, 625–645 (2002)
34. Zhou, G., Davidson, L., Olsson, E.: Transonic Inviscid/Turbulent Airfoil Flow Simulations Using a Pressure Based Method with High Order Schemes. In: Fourteenth International Conference on Numerical Methods in Fluid Dynamics, pp. 372–378 (1995)
35. Stone, H.L.: Iterative solution of implicit approximations of multidimensional partial differential equations. SIAM J. Numer. Anal. **5**(3), 530–558 (1968)
36. Smagorinsky, J.: General circulation experiments with the primitive equations: 1. The basic experiment. Mon. Weather. Rev. **91**(3), 99–164 (1963)
37. Germano, M., Piomelli, U., Moin, P., Cabot, W.H.: A dynamic subgrid-scale eddy viscosity model. Phys. Fluids A: Fluid Dyn. **3**(7), 1760–1765 (1991)

38. Lilly, D.K.: A proposed modification of the Germano subgrid-scale scale closure method. Phys. Fluids A: Fluid Dyn. **4**(3), 633–635 (1992)
39. Fehlberg, E.: Klassische Runge-Kutta-Formeln fünfter und siebenter Ordnung mit Schrittweiten-Kontrolle. Computing **4**, 93–106 (1967)
40. Schäfer, F., Breuer, M.: Comparison of c-space and p-space particle tracing schemes on high-performance computers: accuracy and performance. Int. J. Numer. Methods Fluids **39**, 277–299 (2002)
41. Williams, F.A.: Recent Advances in Theoretical Descriptions of Turbulent Diffusion Flames. In: Turbulent Mixing in Nonreactive and Reactive Flows, pp. 189–208. Springer (1975)
42. Peters, N.: Laminar diffusion flamelet models in non-premixed turbulent combustion. Prog. Energy Combust. Sci. **10**, 319–339 (1984)
43. Peters, N.: Laminar flamelet concepts in turbulent combustion. Symp. (Int.) Combust. **21**(1), 1231–1250 (1988)
44. de Goey, L.P.H., ten Thije Boonkkamp, J.H.M.: A flamelet description of premixed laminar flames and the relation with flame stretch. Combust. Flame **119**(3), 253–271 (1999)
45. van Oijen, J.A.: Flamelet-Generated Manifolds: Development and Application to Premixed Laminar Flames. Dissertation (Ph.D.), Eindhoven University of Technology, Eindhoven (2002)
46. van Oijen, J.A., de Goey, L.P.H.: Modelling of premixed laminar flames using Flamelet-Generated manifolds. Combust. Sci. Technol. **161**, 113–137 (2000)
47. van Oijen, J.A., Lammers, F.A., de Goey, L.P.H.: Modeling of complex premixed burner systems by using flamelet-generated manifolds. Combust. Flame **127**, 2124–2134 (2001)
48. Vreman, A.W., Albrecht, B.A., van Oijen, J.A., de Goey, L.P.H., Bastiaans, R.J.M.: Premixed and non-premixed generated manifolds in large-eddy simulation of Sandia flame D and F. Combust. Flame **153**, 394–416 (2008)
49. Smith, G.P., Golden, D.M., Frenklach, M., Moriarty, N.W., Eiteneer, B., Goldenberg, M., Bowman, C.T., Hanson, R.K., Song, S., Gardiner, W.C. Jr., Lissianski, V.V., Qin, Z.: GRI-Mech 3.0 (http://combustion.berkeley.edu/gri-mech/)
50. Butler, T.D., O'Rourke, P.J.: A numerical method for two dimensional unsteady reacting flows. Symposium (International) on Combustion **16**(1), 1503–1515 (1977)
51. O'Rourke, P.J., Bracco, F.V.: Two scaling transformations for the numerical computation of multidimensional unsteady laminar flames. J. Comput. Phys. **33**, 185–203 (1979)
52. Charlette, F., Meneveau, C., Veynante, D.: A Power-Law flame wrinkling model for LES of premixed turbulent combustion Part I: Non-dynamic formulation and initial tests. Combust. Flame **131**, 159–180 (2002)
53. Légier, J.P., Poinsot, T., Veynante, D.: Dynamically thickened flame LES model for premixed and non-premixed turbulent combustion. In: Center for Turbulence Research. Proceedings of the Summer Program, pp. 157–168 (2000)
54. Durand, L., Polifke, W.: Implementation of the Thickened Flame Model for Large Eddy Simulation of Turbulent Premixed Combustion in a Commercial Solver. In: ASME Turbo Expo Conference Proceedings, pp. 869–878 (2007)
55. Kuenne, G., Ketelheun, A., Janicka, J.: LES Modeling of premixed combustion using a thickened flame approach coupled with FGM tabulated chemistry. Combust. Flame **158**, 1750–1767 (2011)
56. Künne, G.: Large Eddy Simulation of Premixed Combustion Using Artificial Flame Thickening Coupled with Tabulated Chemistry. Ph.D. thesis. TU Darmstadt, Darmstadt (2012)
57. Ketelheun, A., Kuenne, G., Janicka, J.: Heat transfer modeling in the context of large eddy simulation of premixed combustion with tabulated chemistry. Flow Turbul. Combust. **91**, 867–893 (2013)
58. Chem1D: A one-dimensional laminar flame code, developed at Eindhoven University of Technology (http://www.tue.nl/en/university/departments/mechanical-engineering/research/research-groups/multiphase-and-reactive-flows/our-expertise/chem1d/)
59. Somers, B.: The Simulation of Flat Flames with Detailed and Reduced Chemical Models. Dissertation (Ph.D.), Eindhoven University of Technology, Eindhoven (1994)
60. Crowe, C.T., Sharma, M.P., Stock, D.E.: The Particle-Source-ln Cell (PSI-CELL) Model for Gas-Droplet Flows. J. Fluids Eng. **6**, 325–332 (1977)
61. Ranz, W.F., Marshall, W.R.: Evaporation from drops: I. Chem. Eng. Prog. **48**, 141–146 (1952)
62. Ranz, W.F., Marshall, W.R.: Evaporation from drops: II. Chem. Eng. Prog. **48**, 173–180 (1952)
63. Badzioch, S., Hawksley, P.: Kinetics of thermal decomposition of pulverized coal particles. Ind. Eng. Chem. Process. Des. Dev. **9**, 521–530 (1970)
64. Fletcher, T.H., Kerstein, A.R., Pugmire, R.J., Grant, D.M.: Chemical percolation model for devolatilization. 2. Temperature and heating rate effects on product yields. Energy Fuels **4**, 54–60 (1990)

65. Fletcher, T.H., Kerstein, A.R., Pugmire, R.J., Solum, M.S., Grant, D.M.: Chemical percolation model for devolatilization. 3. Direct use of carbon-13 NMR data to predict effects of coal type. Energy Fuels **6**, 414–431 (1992)
66. Grant, D.M., Pugmire, R.J., Fletcher, T.H., Kerstein, A.R.: Chemical model of coal devolatilization using percolation lattice statistics. Energy Fuels **3**, 175–186 (1989)
67. Baum, M.M., Street, P.J.: Predicting the combustion behaviour of coal particles. Combust. Sci. Technol. **3**(5), 231–243 (1971)
68. Field, M.A., Gill, D.W., Morgan, B.B., Hawksley, P.G.W.: Combustion of pulverized coal. British coal utilization research association. leatherhead, UK (1967)
69. Gövert, B., Pielsticker, S., Kreitzberg, T., Habermehl, M., Hatzfeld, O., Kneer, R.: Measurement of reaction rates for pulverized fuel combustion in air and oxyfuel atmosphere using a novel fluidized bed reactor setup. Fuel **201**, 81–92 (2017)